STUDY OF NONLINEAR LANDAU DAMPING AND FORMATION OF BERNSTEIN-GREENE-KRUSKAL STRUCTURES FOR COLLISIONLESS, 1D PLASMAS

A thesis submitted towards partial fulfilment of
BS-MS Dual Degree Programme

by

Madhusudan Raghunathan

under the guidance of

R. GANESH

INSTITUTE FOR PLASMA RESEARCH, GANDHINAGAR, INDIA

Indian Institute of Science Education and Research Pune

Certificate

This is to certify that this thesis entitled "Study of Nonlinear Landau Damping and Formation of Bernstein-Greene-Kruskal Structures for Collisionless, 1D Plasmas" submitted towards the partial fulfillment of the BS-MS dual degree programme at the Indian Institute of Science Education and Research Pune represents original research carried out by Madhusudan Raghunathan at Institute for Plasma Research, Gandhinagar, under the supervision of Dr. R. Ganesh during the academic year 2012-2013.

Student
Madhusudan Raghunathan

Supervisor
Dr. R. Ganesh

Acknowledgments

The candidate would like to firstly thank Dr. R. Ganesh for his invaluable mentorship. The candidate would also like to thank Dr. R. Srinivasan for his insightful inputs regarding various aspects of the Vlasov-Poisson solver. The candidate would also like to thank Dr. P. K. Kaw and Dr. A. Sen for their invaluable assessment of the work. This work was undertaken under the auspices of the KVPY fellowship (SX-1071113). Also, I acknowledge the Institute for Plasma Research (IPR) for the generosity regarding accommodation, use of library, and dissemination of publication fees. Finally, the candidate would like to thank Dr. P. Subramanian for kindly agreeing to help with the coordination of this project with IISER, Pune.

Abstract

In the past, long-time evolution of an initial perturbation in collisionless Maxwellian plasma ($q = 1$) has been simulated numerically. The controversy over the nonlinear fate of such electrostatic perturbations was resolved by Manfredi[G. Manfredi, Phys. Rev. Lett. **79**, 2815-2818 (1997)] using long-time simulations up to $t = 1600\omega_p^{-1}$. The oscillations were found to continue indefinitely leading to BGK-like phase-space vortices (from here on referred to as 'BGK structures'). Using a newly developed, high resolution 1D Vlasov-Poisson solver based on Piecewise-Parabolic Method (PPM) advection scheme, we investigate the nonlinear Landau damping in 1D plasma described by toy q-distributions for long times, up to $t = 3000\omega_p^{-1}$. We show that BGK structures are found only for a certain range of q-values around $q = 1$. Beyond this window, for the generic parameters, no BGK structures were observed. We observe, that for values of $q < 1$ where velocity distributions have long tails, strong Landau damping inhibits the formation of BGK structures. On the other hand, for $q > 1$ where distribution has a sharp fall in velocity, the formation of BGK structures is rendered difficult due to high wave number damping imposed by the steep velocity profile, which had not been previously reported. Wherever relevant, we compare our results with past work.

Contents

Chapter 1

Introduction

1.1 Landau Damping

Collisionless plasmas, by definition, do not have a significant number of inter-particle collisions. Because of this, one would not expect the dissipation of energy. For a dissipational system, such as an oscillating pendulum being slowed down by air resistance, we would expect the initial energy of the pendulum to be eventually dissipated away to the surrounding medium, and the pendulum never regains its original amplitude of oscillation. However, collisionless plasmas, by the virtue of consisting of two oppositely-charged species, are able to store some of the dissipated energy as the potential energy of that plasma. This is also the reason that plasma oscillations occur, where the particles keep exchanging energy of the field periodically, sustaining a steady oscillation in the electric field. By similar mechanism, the particles, which are more or less stationary in the frame of perturbation, can resonantly interact with the field in such a manner that they absorb energy from the field and cause the oscillations to damp away. This collisionless damping is known as Landau damping[1, 2]. For collisionless plasmas, where dissipation by collisions is negligible, the damped oscillations may resurge in their full amplitude, if triggered with an appropriately phased disturbance. This phenomenon is known as a plasma echo[3]. Particles may also interact with the electric field to form pockets of trapped particles in the phase-space, due to trapping nonlinearity, leading to coherent structures in phase-space known as Bernstein-Greene-Kruskal (BGK) structures.

The kinetic theory presents a useful way to several such phenomena in plasma physics. It involves studying processes in terms of the distribution function and the effect of the different physical quantities, such as the electric field, on it. One example of the application of kinetic theory is for collisionless plasma, where the inter-particle collisions can be neglected.

For collisionless plasma, which will be our concern throughout, the kinetics of the plasma are described by the Vlasov-Poisson equation system. For one dimensional, col-

lisionless plasma, the Vlasov-Poisson equations[2] are:

$$\frac{\partial f}{\partial t} + v\frac{\partial f}{\partial x} - \frac{eE}{m_e}\frac{\partial f}{\partial v} = 0 \tag{1.1}$$

$$\frac{\partial E}{\partial x} = \frac{e^2}{m_e \epsilon_0}\left(n_0 - \int f dv\right) \tag{1.2}$$

where $f = f(x, v, t)$ is the electron distribution function, $E = E(x, t)$ is the electric field, n_0 is the number density of the neutralizing ion background. (Rest of the symbols have their usual meaning).

One can notice that Eq. (1.1) does not have non-zero RHS. This means that there are no sources or sinks, such as the ones created by collisions of particles, present in the system which could lead to dissipation or growth of kinetic energy. Therefore one would usually not expect an applied perturbation to damp away.

In order to study how an infinitesimal perturbation behaves in a collisionless plasma, we need to perturb the distribution function with a small perturbation in (x, v). One can see from Eq. (1.1), that a perturbation in x-domain would soon phase-mix and cause a perturbation in v-domain. Thus, we need the perturbation to reflect the change of the distribution in both x- and v-domain. On substituting the infinitesimal perturbation, $f(x, v, t) = f_0(v) + f_1(x, v, t)$ and $E(x, t) = E_1(x, t)$ (where $E_0(x)$ is assumed to be zero for no initial background electric field), and retaining the terms up to first order only, we get the linearized system:

$$\frac{\partial f_1}{\partial t} + v\frac{\partial f_1}{\partial x} - \frac{eE_1}{m_e}\frac{\partial f_0}{\partial v} = 0 \tag{1.3}$$

$$\frac{\partial E_1}{\partial x} = -\frac{e^2}{m_e \epsilon_0}\int f_1 dv \tag{1.4}$$

Also, on perturbing the plasma, the plasma will exhibit plasma oscillations caused by the formation of a periodic charge density. Therefore, the perturbed distribution will have a wave-like behaviour. Therefore, on choosing the ansatz $f_1, E_1 \sim \exp i(kx - \omega_i t)$ (where ω_i is complex, given by $\omega_i = \omega + i\gamma$), the system can be reduced to the following dispersion relation:

$$1 = -\frac{e^2}{km\epsilon_0}\left(\int \frac{\partial f_0/\partial v}{\omega_i - kv}\, dv\right) \tag{1.5}$$

The complex angular frequency makes sure that we account for both continuing oscillations and the damping/growth of the oscillations.

Landau, in 1946, noticed that one had to correctly account for a singularity at $kv = \omega_i$ in the complex velocity plane[1]. Within the linear limit, where $k << 1$, such that $\gamma < 0$ and $|\gamma/\omega| \ll 1$, the dispersion relation can be approximated, by contour integration, to get:

$$\omega_i = \omega_p\left(1 + i\frac{\pi}{2}\frac{\omega_p^2}{k^2}\left[\frac{\partial \hat{f}_0}{\partial v}\right]_{v=v_\phi}\right) \tag{1.6}$$

where $\hat{f}_0$ is the normalized equilibrium distribution function and $kv_\phi = \omega + i\gamma$. λ_D is the Debye length given by $\lambda_D = \sqrt{\frac{\epsilon_0 k_B T}{n_0 e^2}}$, the thermal velocity v_{th} is $v_{th} = \sqrt{\frac{k_b T}{m}}$ and the plasma frequency ω_p is given by $\omega_p = \sqrt{\frac{n_0 e^2}{m_e \epsilon_0}}$. For an initial Maxwellian $f(v) = (\pi v_{th}^2)^{-1/2} \exp(-v^2/v_{th}^2)$, the damping rate γ, is found to be:

$$\gamma = \mathrm{Im}\left(\frac{\omega_i}{\omega_p}\right) \approx -0.22\sqrt{\pi}\left(\frac{\omega_p}{k v_{th}}\right)^3 \exp\frac{-1}{2k^2\lambda_D^2} \tag{1.7}$$

Therefore, once can see that the initial perturbation is damped away despite there being no dissipative term in the RHS of the Vlasov equation. However, for a finite value of k or for large amplitude of perturbation, the approximation of γ being small may not be valid. From the linearization process, we can notice that linear Landau damping is only occurs till the contribution of the nonlinear term in the Vlasov equation, i.e. $(-eE_1/m_e)(\partial f_1/\partial v)$, becomes significant. Once this term is comparable to rest of the terms in the Vlasov equation, the behaviour of the system becomes nonlinear.

Attempts at an analytical solution to nonlinear Landau damping have met only with limited success. However, the Vlasov-Poisson equation system can be solved numerically to understand the dependence of the nonlinear behaviour on different types of initial perturbations. We now move to explain a brief history of the study of such analytical and computational efforts. We also introduce the succinct essentials of our work.

1.2 Recent Work in Nonlinear Landau Damping (1997-2012)

Summarizing the previous section: Exponential damping of small vibrations in uniform, one-dimensional, Maxwellian, collisionless, electronic plasma was first pointed out by Landau by correctly accounting for the singularity in the contour integral for the dispersion relation[1]. It meant that damping occurs in a perturbed plasma despite the absence of any dissipative term. Since then, this phenomenon has been shown in innumerable simulations for collisionless plasmas. Landau's treatment is restricted to infinitesimal perturbations, which helps approximate the system to be linear. This helps simplify the system and, from there on as shown in the previous section, is solved rigorously.

However, as the amplitude of perturbation becomes larger, contribution from the nonlinear terms become more significant and the behaviour deviates from uniform exponential damping. The approximate analytical solutions available for nonlinear damping are not valid for long-times. For example, O'Neil analytically showed that the system undergoes oscillations with trapping time τ as the period, and that the damping rate goes to zero with times much greater than the trapping time[4]. However, O'Neil's treatment is not applicable for times much greater than the trapping time.

For a many decades, the fate of nonlinear finite amplitude electrostatic perturbations for times much greater than O'Neil trapping time was an open problem. The question of whether electrostatic perturbations will damp away at $t \to \infty$ or whether it would lead to

the formation of Bernstein-Greene-Kruskal (BGK)[5] structures was hotly debated. For example, in 1997, Isichenko proposed that such perturbations undergo Landau damping following an algebraic decay[6]. However, this derivation itself was under the assumption of decay of the field. Manfredi observed from long-time numerical simulations up to $1600\omega_p^{-1}$ that, for a finite amplitude perturbation, the plasma undergoes a few amplitude oscillations (O'Neil oscillations) and then approaches a steady-state[7] similar to BGK mode. Soon after, in 1998, Lancelotti and Dorning showed that Isichenko analysis was erroneous in that the final damping rate obtained did not satisfy an assumption made early on in the analysis [8]. Furthering this debate, in 2000, Firpo and Elskens proposed a Hamiltonian model where in it was shown that there exists a critical wave-intensity above which Landau damping leads to a finite field amplitude, and below which equilibrium amplitude vanishes[9]. Later in 2004, Ivanov, Cairns and Robinson, using Vlasov simulations, have also found the existence of such a critical perturbation amplitude[10]. Further, in 2009, Barré and Yamaguchi, using a Hamiltonian mean-field model, have shown that systems with repulsive interactions, such as plasmas, can indeed sustain long-lasting small travelling clusters, and have discussed the existence of an upper limit on the value of the perturbation amplitude for which trapping occurs[11].

However, these studies were for Maxwellian plasmas. As is well known, Maxwellians may not adequately describe systems with long-range interactions, especially collisionless systems such as gravitational systems and plasmas. It is also well-known that for a system with short range interactions, the energy of the system is additive or extensive. Therefore, maximizing Boltzmann-Gibbs-Shannon (BGS) entropy under energy constraints leads to a Maxwellian.

In the past, linear Landau damping[12] has been studied for non-Maxwellian distributions. Also, for non-Maxwellian distributions, existence localized steady-state structures has been found [13] using pseudo-potential method, first developed by Schamel [14]. Also, for systems which interact with long-range interactions and for which energy is not additive or extensive, deviations from BGS statistics have been attempted leading to non-extensive generalizations.

One class of non-Maxwellian distributions are the q-distributions, which have a broad range of applicability. Tsallis, in 1998, introduced the q-nonextensive entropy functional[15]:

$$S_q = \int_0^L \int_{-\infty}^{+\infty} f(x,v) \left(\frac{1 - f(x,v)^{q-1}}{q-1} \right) \, dv \, dx. \tag{1.8}$$

where q is the strength of nonextensivity. The corresponding q-distribution is derived as an extremum state of this new entropy functional[16]:

$$f_q(v) = C_q \left[1 - (q-1) \left[\frac{v^2 - e\phi_0/m_e}{2v_{th}^2} \right] \right]^{1/(q-1)} \tag{1.9}$$

where ϕ_0 denotes the electric potential. The normalization constant C_q is given by:

$$C_q = \begin{cases} n_0 \frac{\Gamma\left(\frac{1}{1-q}\right)}{\Gamma\left(\frac{1}{1-q} - \frac{1}{2}\right)} \sqrt{\frac{1-q}{2\pi v_{th}^2}} & \text{for } -1 < q < 1 \\ n_0 \left(\frac{1+q}{2}\right) \frac{\Gamma\left(\frac{1}{q-1} + \frac{1}{2}\right)}{\Gamma\left(\frac{1}{q-1}\right)} \sqrt{\frac{q-1}{2\pi v_{th}^2}} & \text{for } q > 1 \end{cases} \tag{1.10}$$

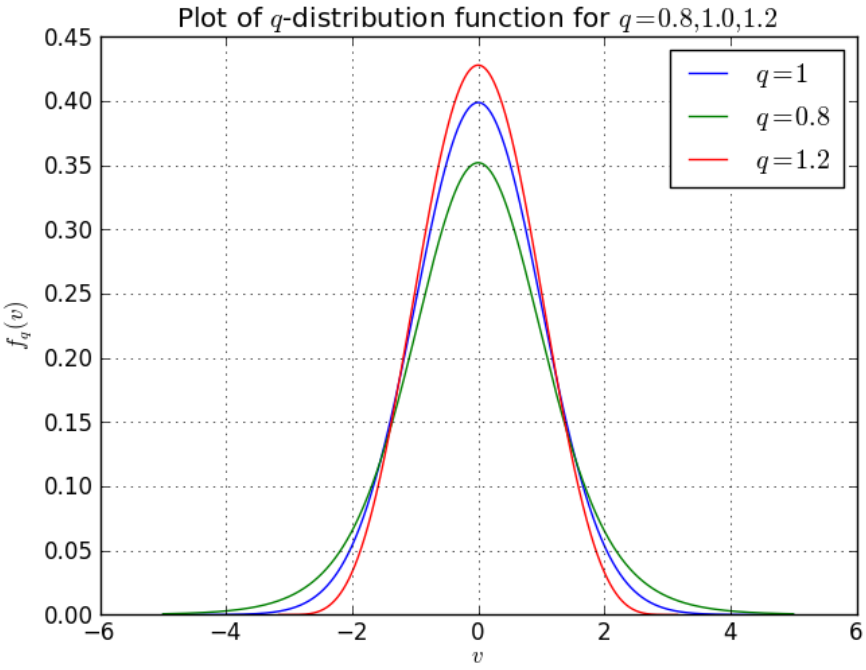

Figure 1.1: Plot of the q-distribution function for values $q = 0.8, 1.0, 1.2$.

Under the limit of $q = 1$, the entropy functional reduces to BGS entropy $S_1 = \int\int f \ln f \, dxdv$, and the q-distribution $f_1(v)$ reduces to a normalized Maxwellian. The distributions, for decreasing $q < 1$, have longer tails and lower peaks. For increasing $q > 1$, these distributions have shorter tails and higher peaks. As one can see from Eq. (1.9), $q > 1$ distribution functions exhibit a velocity cutoff at $v_{\text{cutoff}} = \sqrt{2/(q-1)}$. We can see these properties in Fig. 1.1. One can notice that $f_{1.2}$ has a velocity cutoff at $v \approx 3.16$. We shall explore the significance of the velocity cutoff in the simulations performed.

We must mention that there is nothing unique about S_q. However, it has been found that q-distributions lend themselves to applications in vast number of problems in plasmas[17, 18]. The q-distribution has also been able account for the velocity distributions of gravitational systems such as galaxy clusters[19].

The trapping of particles for nonlinear Landau damping in q-distributions has been studied in the past[20]. However, these simulations performed were for relatively smaller deviations around $q = 1$, for gridsizes smaller than Manfredi's simulations and for times up to $1200\omega_p^{-1}$. Also, this work[20] is exclusively concerned with the dependence of trapping of particles on perturbation amplitude and the resulting bounce time. In this work, it is argued that the effect of increasing damping rate and bounce time with decreasing value of q limits trapping for $q < 1$ whereas trapping is efficient for $q > 1$.

However, to the authors's knowledge, the phenomenon has not been studied for variations of perturbation wavenumber and its effect on limiting the range of q for which such trapping can be found. We explore the presence of BGK structures over a broader range of q around $q = 1$ and determine numerically the extent to which trapping depends

on the value of perturbation wavenumber. The simulations undertaken have been run till $3000\omega_p^{-1}$ on gridsizes comparable to Manfredi's simulations. In the case of $q > 1$, we also find that simulations till $1200\omega_p^{-1}$ do not let the numerical entropy settle to a stable value, hence making it necessary to prolong the simulations in order to confirm a numerical steady-state. This, for $q < 1$, brings to our attention a new behaviour of the system. On extending the simulations, we confirm that the increasing damping rate with decreasing q puts a lower limit on q beyond which no trapping occurs. This confirms Valentini's findings for $q < 1$[20]. We find additionally that, for $q > 1$, damping is restricted by an upper limit on the perturbation wavenumber k, which in turn imposes an upper limit on the value of q for trapping, which was previously not addressed.

We now proceed to describe the construction of the Vlasov-Poisson solver in the next section.

Chapter 2

Numerical Solution of the Vlasov-Poisson Equations

We first construct a numerical solver that can self-consistently solve both the Vlasov and Poisson equations and advance the solution in time. A one-dimensional, collisionless plasma can be modelled using the Vlasov-Poisson system, given by:

$$\begin{aligned} \frac{\partial f}{\partial t} + v\frac{\partial f}{\partial x} + E\frac{\partial f}{\partial v} &= 0 \\ \frac{\partial E}{\partial x} &= \int f \, dv - 1 \end{aligned} \tag{2.1}$$

where $f(x, v, t)$ is the electron distribution function and $E(x, t)$ is the electric field. For this system, time has been normalized to the plasma frequency ω_p, space has been normalized to the Debye length λ_D, velocity has been normalized by $v_{th} = \lambda_D \omega_p$. Consequently, f gets normalized by n_0/v_{th} and E by $-m_e v_{th}^2/e\lambda_D$. In this model, the ions form a stationary neutralizing background of number density n_0. Hence, the numerical value of '1' in the Poisson equation. One can see that any unperturbed normalized velocity distribution function, in the absence of a background electric field, is a solution of the Vlasov-Poisson system.

In order to solve Eq. (2.1), we use the time-stepping method suggested by Cheng and Knorr[21]. We apply the following time-stepping for one time step Δt:

- Solve $\partial f/\partial t + v\partial f/\partial x = 0$ for $\Delta t/2$, for a given v in the v-domain.
- Solve the Poisson equation to obtain $E(x)$
- Solve $\partial f/\partial t + E\partial f/\partial v = 0$ for Δt, for an E in the obtained $E(x)$
- Again, solve $\partial f/\partial t + v\partial f/\partial x = 0$ for $\Delta t/2$, for a given v in the v-domain.

Thus, the solution of the system is reduced to solving two 1D advection equations and a Poisson equation. This method formally incurs an error of the order $O((\Delta t)^3)$. Further, this requires a reliable advection solver and a Poisson solver. There are several methods

of implementing this time-stepping method depending on how one chooses to evolve the advections[22]. We select an Eulerian fixed grid advection scheme for the solution of the advection equation. The advantage of doing so is that the advections are constant speed advections, for which various methods are available. Some of the advection methods are, for example, are flux-balance(FB) method[23, 22], piecewise parabolic method (PPM)[24, 22] and flux-corrected transport (FCT) method[25, 22].

Arber and Vann[22] have performed a comparison of various advection solvers with regards to parameters like monotonicity preservation, positivity of the distribution function, etc. They found on this basis that lower order methods like the flux-balance method were too coarse for the accuracy required. On the other end, they found that the finest advection solver, the flux-corrected transport engaged in truncation of the distribution function (which implies loss of information during the solution). However, the piecewise-parabolic(PPM) advection method was found to be sufficiently fine, while not causing an alarming loss of information. Therefore, we chose PPM advection method as our advection solver. The PPM advection method is formally third-order accurate away from the extrema and first-order accurate at the extrema. Also, the monotonicity limiters of the PPM method ensure that the positivity of the distribution function is maintained. Also, a Fourier transform based solution is employed for the Poisson equation, described in section 2.2.

2.1 Piecewise Parabolic Method (PPM) Advection Solver

Let us consider a general advection equation,

$$\frac{\partial a}{\partial t} + u\frac{\partial a}{\partial \xi} = 0 \tag{2.2}$$

where $a = a(\xi, t)$ is the function being advected and $u = u(\xi, t)$ is the constant velocity by which the function a is advected, and ξ, u are the generalized coordinates. The initial value for the problem is set as $a(\xi, 0) = a_0(\xi)$. u may also be a function of a, in case of which the advection equation would be nonlinear. To solve the advection equation, we apply the method outlined by Colella and Woodward[24]:

1. The value of the discretized function a_j^n (where n is the timestep and j is the position step) is defined as the zone average of the underlying function $a(\xi, t^n)$, over the cell:

$$a_j^n = \frac{1}{\Delta\xi_j}\int_{\xi_{j-1/2}}^{\xi_{j+1/2}} a(\xi, t^n)d\xi \tag{2.3}$$

   where $\Delta\xi_j = \xi_{j+1/2} - \xi_{j-1/2}$, where $\Delta\xi_j$ represents the cell size and $\xi_{j+1/2}$,$\xi_{j-1/2}$ represent the cell edges.

2. Now, the underlying function is defined to be a piecewise parabola[24], as follows:

$$a(\xi) = a_{L,j} + x(\Delta a_j + (1-x)a_{6,j}) \tag{2.4}$$

where $x = (\xi - \xi_{j-1/2})/\Delta\xi_j$, where $\xi_{j+1/2} \leq \xi \leq \xi_{j-1/2}$. Now, the solution is just advection along the characteristics of the problem, given by:

$$a_j^{n+1} = \frac{1}{\Delta\xi_j} \int_{\xi_{j-1/2}}^{\xi_{j+1/2}} a(\xi - u\Delta t) d\xi \tag{2.5}$$

where $\Delta a_j = a_{R,j} - a_{L,j}$, and $a_{R,j} = a(\xi_{j+1/2}, t^n)$ and $a_{L,j} = a(\xi_{j-1/2}, t^n)$ are the values of a at the cell edges. On substituting the piecewise parabolic function in the above equation, one gets a constraint:

$$a_{6,j} = 6(a_j^n - 0.5(a_{R,j} + a_{L,j})) \tag{2.6}$$

3. Now we notice that the indefinite integral $A(\xi) = \int^{\xi} a(\xi', t^n) d\xi'$ can be given by:

$$A(\xi_{j+1/2}) = A_{j+1/2} = \sum_{k \leq j} a_k^n \Delta\xi_k \tag{2.7}$$

To define A, one interpolates a quartic polynomial between 5 points, spaced around $a(\xi_{j+1/2})$, and uses the relation:

$$a_{j+1/2} = \left(\frac{dA}{d\xi}\right)_{j+1/2} \tag{2.8}$$

to obtain a value for $a_{R,j}$. Also, $a_{L,j}$ is set to be the value of $a_{R,j-1}$.

4. Once the interpolated cell-edge values are defined, one applies a monotonicity condition. Now, if a_j^n were the extremum, then the values of $a_{R,j}$ and $a_{L,j}$ are reset to the value of a_j^n. Now, if $a(\xi)$ achieved an extremum somewhere in the cell, then depending on where the extremum is close to, then one of the cell-edges is is reset in such a way, so that the derivative at that cell edge is zero. This procedure maintains monotonicity of a.

5. Additionally, the values of $a_{R,j}$ and $a_{L,j}$ are reset depending on whether a discontinuity is detected. The discontinuity is detected as per a user given tolerance, and this modifies the cell-edge function values to preserve the discontinuity during advection.

6. Now that we have all the required parameters, we advect the function as (2.5) would define it.

The PPM advection solver is third-order accurate away from the extrema and first-order accurate at the extrema[22]. Note that PPM advection solver is explicit in nature and hence has to obey the Courant-Frederichs-Löwy(CFL) condition:

$$k = \left|\frac{u\Delta t}{\Delta\xi}\right| \leq 1 \tag{2.9}$$

However, if Δt happens to have a value that violates this condition, then there are ways to avoid the restriction set forth by the CFL condition. For example, one can displace the solution by an integral number of grid points, such the remainder of the timestep left would satisfy the CFL condition[22]. This is correct because, analytically, we have:

$$a(\xi, t + \Delta t) = a(\xi - u\Delta t, t) \tag{2.10}$$

and when $u\Delta t = p\Delta x$, where the CFL number p is an integer then:

$$a(\xi, t + \Delta t) = a(\xi - p\Delta x, t) \tag{2.11}$$

As any CFL number can expressed as a sum of an integer and a number in the interval $(0, 1)$, we would shift the solution to the right by number of gridpoints equal to that integer and would apply PPM for the remainder of the time (in which case $k \in (0, 1)$). However one has to be aware that even though, by using this trick, a larger timestep may not affect the advection solver, it does contribute to the $O((\Delta t)^3)$ error in the Strang splitting[30]. The PPM advection solver has been thoroughly benchmarked in Appendix A. Next, we obtain methods to solve the Poisson equation.

2.2 Solution of the Poisson Equation using Fourier Transforms

The Poisson equation is:

$$\frac{\partial E(x)}{\partial x} = \rho(x) \tag{2.12}$$

where $\rho = \int f \; dv - 1$, in our case. On performing a Fourier transform, we get:

$$ik\tilde{E}(k) = \tilde{\rho}(k) \tag{2.13}$$

where k is the conjugate variable to x and $\sim$ represents the transform of the original variable into k-space. Therefore:

$$\tilde{E}(k) = -i\frac{\tilde{\rho}(k)}{k} \tag{2.14}$$

On performing an inverse Fourier transform, we obtain $E(x)$:

$$E(x) = FT^{-1}\left(-i\frac{\tilde{\rho}(k)}{k}\right) \tag{2.15}$$

where FT^{-1} represents the inverse Fourier transform. Also, we compare this method to the conventional method[31], where:

$$E(x) = FT^{-1}\left(\frac{-i\tilde{\rho}(k_m)}{\sin\frac{2\pi m}{M}}\right) \tag{2.16}$$

where m is the m^{th} harmonic and M is the gridsize of E. In our programs we use FFTW 3.2[48] for performing the Fourier transforms. This reduces the number of operations and makes this method viable as compared to conventional integrators for ODEs. Note that Fourier transform based methods only work for functions $\rho(x)$ with periodic boundary conditions. Furthermore, the solutions may have to be corrected by an additive constant. This additive constant is fixed by the one given boundary condition (on either boundary) on $E(x)$. In case of the Poisson solver in our Vlasov-Poisson solver, where periodic boundary conditions are applied and no additional value is specified, we do not calculate an additive constant to add. For the sake of nomenclature, we call the solution by expression (2.15) as 'Method I' and by (2.16) 'Method II.' Both of these methods are compared and benchmarked in Appendix A.

2.3 Integrator

In order to perform the integration $\int f \, dv$, we use the conventional trapezoidal rule[32]:

$$\text{Area} = \frac{L_v}{N} \sum_{i=1}^{n} f_i \tag{2.17}$$

assuming that the function f is discretized over equally spaced n points with periodic boundary conditions (such that $f_{n+1} = f_1$). Also, $L_v/n(= h)$ represents the stepsize in v. The theoretical error is $(L_v^3/12N^2) \max(f'')$, which roughly corresponds to $O(h^3)$.

Now that the individual components have been benchmarked, We assemble the solver. We proceed to explain how the solver is assembled and introduce some features of the solver.

2.4 Choice of Timestep and The Large Timestep Algorithm

The first problem, in assembling a functional Vlasov-Poisson solver, is the choice of the timestep. PPM advection solver, being an explicit advection method, is bound by the CFL condition $|v\Delta t/\Delta x| \leq 1$. Thus, one can choose the timestep such that the maximum CFL number during the advancement of one timestep, does not violate this. Thus we choose Δt such that:

$$\Delta t = \min\left(\frac{\Delta x}{v_{max}}, \frac{\Delta v}{\max|E|}\right) \tag{2.18}$$

where v_{max} is the value of maximum velocity on the velocity grid and $\max|E|$ is the maximum absolute value of the electric field. $\Delta x, \Delta v$ are the sizes of the steps on the x and v grid. We will often refer to this choice as the "regular timestep algorithm." Now, this leads to smaller timesteps as gridsize increases. The computational time is affected because of both larger time required to solve one timestep and requirement of more timesteps to solve up to the same time, with larger gridsize. But, we have a workaround,

when we solve the individual advection algorithms. We can define a value of Δt in the beginning. Then, we define an integer p such that:

$$p = \begin{cases} \left\lfloor \frac{v\Delta t}{\Delta x} \right\rfloor & v \geq 0 \\ \left\lfloor \frac{v\Delta t}{\Delta x} \right\rfloor + 1 & v < 0 \end{cases} \tag{2.19}$$

where $\lfloor \rfloor$ refers to the floor function (the greatest integer less than the argument). Remember that CFL number $k = 1$ represents the shift of the advected function by one gridpoint to the right. Thus, depending on whether we are performing advection in x or v domain, we shift the grid by p to the right in x or v respectively. That is:

$$\begin{aligned} a(x_m, v_n, t) &\leftarrow a(x_{m-p}, v_n, t) \quad \text{for advection in } x \\ a(x_m, v_n, t) &\leftarrow a(x_m, v_{n-p}, t) \quad \text{for advection in } v \end{aligned} \tag{2.20}$$

This is equivalent to an advection of p number of Δx or Δv respectively. Now, the remainder of the advection will obey the CFL condition, and the time δt for advection by PPM can be defined as:

$$\begin{aligned} \delta t &= \Delta t - p\frac{\Delta x}{v} \quad \text{for advection in } x \\ \delta t &= \Delta t - p\frac{\Delta v}{E} \quad \text{for advection in } v \end{aligned} \tag{2.21}$$

We perform advection by δt by using PPM advection routine, and this would not violate the CFL condition. We refer to it in the text as the "large timestep algorithm." Also, any round-off error propagated by the large timestep algorithm is overshadowed by the intrinsic errors caused by PPM. Thus, this is a viable method to use larger timesteps.

2.5 Assembly of the Vlasov-Poisson Solver

Now that the timestep has been decided, we set up other initial conditions, such as the distribution function. Also, as seen in the previous section, we choose Method I for the solution of the Poisson equation. Then, we use the Cheng-Knorr timestepping method and perform the following:

- Apply PPM routine for half timestep $\Delta t/2$ in x-domain, for various constant v.
- Apply Poisson FFT routine to get the electric field. Use the integrator to get the initial conditions for this routine.
- Apply PPM for a full timestep Δt in v-domain, for various constant E, obtained from the previous step.
- Apply PPM routine for another half timestep $\Delta t/2$ in x-domain, for various constant v.

for advancement in one timestep Δt, as mentioned before. This method is formally known as Strang splitting and has a theoretical error of $(O((\Delta t)^3))$. Also, various diagnostics are put at the end of each timestep to study various properties of the solver. We describe them in the next subsection.

2.6 Some Additional Features of the Vlasov-Poisson Solver

Some additional features that act as diagnostics and failsafes have been implemented in the Vlasov-Poisson solver. Diagnostics help us study the accuracy and physicality of the solutions. Failsafes help the solver fail in a reliable manner, in case it happened to fail.

1. **An Integrator package:** Given that the distribution $f(x_m, v_n)$ is a 2d array, we have implemented an integrator package that accounts for all integrations needed by various parts of the program.

2. **A Write Package:** A package has been written for performing file writing functions. This package contains functions for writing files for a quantity at one particular timestep, and for writing files for quantities that are solely a function of time.

3. **A Restart algorithm:** An algorithm has been written to restart the program in case of an interruption. This leverages the write package to write files at regular intervals. On restart the user must specify the time of interruption, and this algorithm reads the concerned files and loads those quantities to restart the program mid-way. The restart algorithm is a failsafe for simulations which require large CPU-time.

4. **Diagnostics:** We have built in several diagnostics for the solver. These include diagnostics for:

   - Total energy $E_{total}(t)$, given by: $E_{total}(t) = T(t)+V(t) = (1/2)(\int\int dx\, dv\, v^2 f(x,v,t)+ \int dx\ (E(x,t))^2)$, and momentum $p(t)$, given by: $p(t) = \int\int dx\ dv\ v f(x,v,t)$. The conservation of $E_{total}(t)$ and $p(t)$ is a prime concern for the solver.
   - Numerical entropy S, given by: $S = -\int\int dx\ dv\ f \ln f$.
   - Harmonics of the Electric Field $|E_k|$, by calculating the k^{th} value of the Fourier transform of the electric field, then calculating the modulus of that value.
   - Maximum value of the electric field $E_{\max}$, which is required for those cases when a qualitative representation of the change of electric field with time is needed.

   In addition to these, we store the distribution function f and calculate the corresponding contour plots as a diagnostic tool to understand the nature of f at different times.

As one can notice, these diagnostics may need to leverage other packages or algorithms for their functioning.

Now that we have assembled the solver, we proceed to benchmark the solver to known physical results from linear Landau damping and then apply the solver for long-time simulations for nonlinear Landau damping.

Chapter 3

Simulations

In order to simulate Landau damping, following Manfredi[7], we perturb the distribution function with one Fourier mode. Therefore, we initialize the following distribution function:

$$f(x, v, 0) = (1 + \alpha \cos(kx)) f_{q_0}(v) \tag{3.1}$$

where $f_{q_0}(v)$ is the initial q-nonextensive velocity distribution function. The normalized q-nonextensive velocity distribution function[17] is given by:

$$f_{q_0}(v) = C_q \left[1 - (q-1)\frac{v^2}{2}\right]^{1/(q-1)} \tag{3.2}$$

where q is the strength of nonextensivity and C_q is the normalization constant given by:

$$C_q = \begin{cases} \frac{\Gamma\left(\frac{1}{1-q}\right)}{\Gamma\left(\frac{1}{1-q}-\frac{1}{2}\right)}\sqrt{\frac{1-q}{2\pi}} & \text{for } -1 < q < 1 \\ \left(\frac{1+q}{2}\right)\frac{\Gamma\left(\frac{1}{q-1}+\frac{1}{2}\right)}{\Gamma\left(\frac{1}{q-1}\right)}\sqrt{\frac{q-1}{2\pi}} & \text{for } q > 1 \end{cases} \tag{3.3}$$

where $\Gamma(n)$ represents the standard gamma function. Also, for $q > 1$, the distribution exhibits a velocity cutoff given by $|v_{\text{cutoff}}| = \sqrt{2/(q-1)}$. For $q = 1$, this distribution reduces to the Maxwellian with $C_1 = 1/\sqrt{2\pi}$.

The independent parameters are the strength of perturbation α, the wave number k and the nonextensive parameter q. In addition, we also consider the bounce time $\tau = \alpha^{-1/2}$, after which the linear solution breaks down and nonlinear effects become prominent. (The bounce time τ is the time in which nonlinear trapping becomes important[4].) Therefore, we have developed a nonlinear Vlasov-Poisson solver in order to study this phenomenon for times $t \gg \tau$.

For the present problem, we use the following parameters: We set $L = 2\pi/k$. Throughout the simulations performed, unless mentioned otherwise, we set the strength of perturbation $\alpha = 0.05$ and $k = 0.4$. For the amplitude considered, the bounce time $\tau \approx 4.47$. We also choose $\Delta t = 0.1$, in accordance to the Shannon theorem[26].

With the independent parameters chosen, we now proceed to benchmark the solver in the linear phase of Landau damping. We do so, as to understand the dependence of

the effects of the independent parameters on the short time solution of Landau damping. This helps guage the correctness of the solver, and also lets us independently judge the limitations the physics of the problem imposes on the solver.

3.1 Benchmarking the Vlasov-Poisson solver for linear Landau damping.

We have thoroughly benchmarked the solver in linear phase and the nonlinear phases for Maxwellian distributions, in Appendix B, for test problems in linear Landau damping and Bump-on-Tail instability. However in order to benchmark the correctness of our Vlasov-Poisson solver for an arbitrary velocity distribution function, we have developed a numerical solver for the dispersion relation[27] for linear Landau damping, which we will describe in this section.

In the past, analytical solutions for the dispersion relation of linear Landau damping for κ-distributions (where $\kappa = 1/(1-q)$) have been carried out in terms of special functions, by Valentini and D'Agosta [28]. However, these solutions were constructed for linear Landau damping under the weakly damped limit, where $|\gamma/\omega| \ll 1$. As the damping rate increases, we find that analytical solutions relying on this assumption deviate significantly from the observed values. Therefore, we have developed a dispersion relation solver valid for arbitrary values of $|\gamma/\omega|$. We also look at the results of our dispersion relation solver for the weakly damped case and compare it with Valentini and D'Agosta as an additional benchmark.

We solve the Ampere equation instead of the Poisson equation in order to replicate the results obtained previously by Vann[27]. In principle, the solution of either of the Poisson equation or the Ampere equation should exhibit the same results. Showing that the results obtained from solving the Ampere equation analytically and those obtained from solving the Poisson equation numerically are in agreement would validate the accuracy of the solver from an independent method of solution.

The normalized Vlasov-Ampere system is given by

$$\begin{aligned} \frac{\partial f}{\partial t} + v\frac{\partial f}{\partial x} + E\frac{\partial f}{\partial v} &= 0 \\ \frac{\partial E}{\partial t} &= -\int v f \; dv. \end{aligned} \tag{3.4}$$

We first linearize the Vlasov-Ampere system of equations by choosing $f(x,v,t) = f_{q_0}(v) + f_1(x,v,t)$, and similarly $E(x,t) = E_0(x) + E_1(x,t)$, where the subscript '0' refers to the unperturbed equilibrium solution and the subscript '1' refers to the perturbed correction. At $t = 0$, we assume that the zeroth order or equilibrium electric field to be zero, i.e. $E_0(x) = 0$. Then, we choose ansatz: $f_1, E_1 \sim \exp i(kx - (\omega + i\gamma)t)$, where we have chosen a general angular frequency $\omega + i\gamma$, where ω and γ are real. Substituting the obtained expression for f_1 from the Vlasov equation to the Maxwell equation results in

the following dispersion relation:

$$-\omega - i\gamma = \int_{-\infty}^{+\infty} \frac{v(\partial f_{q_0}/\partial v)}{(kv-\omega) - i\gamma} dv \tag{3.5}$$

The real and the imaginary parts can be separated to obtain:

$$O(\omega,\gamma) \quad : \quad \int_{-\infty}^{+\infty} \frac{(kv-\omega)v(\partial f_{q_0}/\partial v)}{(kv-\omega)^2+\gamma^2} dv - \mathrm{Im}(z) - \omega = 0 \tag{3.6}$$

$$G(\omega,\gamma) \quad : \quad \int_{-\infty}^{+\infty} \frac{\gamma v(\partial f_{q_0}/\partial v)}{(kv-\omega)^2+\gamma^2} dv + \mathrm{Re}(z) - \gamma = 0 \tag{3.7}$$

where:

$$z = \begin{cases} 0 & \text{for } \gamma > 0 \\ 2\pi \left(v \frac{\partial f_{q_0}}{\partial v} \right)_{v=v_{\phi i}} & \text{for } \gamma < 0 \end{cases} \tag{3.8}$$

and where the complex phase velocity $v_{\phi i}$ is given by $kv_{\phi i} = \omega + i\gamma$. We numerically solve for both $O(\omega,\gamma)$ and $G(\omega,\gamma)$ simultaneously to arrive at the analytical value of ω and γ to required tolerance[27].

For a given initial equilibrium distribution function $f_{q_0}(v)$ and a value of k, a domain for ω and γ is chosen. These domains are divided into, say, N equally spaced parts, thus creating N^2 cells on the (ω,γ) grid. Then, the values of LHS of $O(\omega)$ and $G(\gamma)$ are calculated over each point on the (ω,γ) grid. The solution lies in cell in which the curve for the zeroes for $O(\omega,\gamma)$ and $G(\omega,\gamma)$ intersect. For this purpose, it is required to search for cells for which both the LHS of $O(\omega,\gamma)$ and $G(\omega,\gamma)$ have different signs on the corners of the cell. Once such a zone has been obtained, it is further divided into N^2 cells and the procedure is repeated in order to get the solution with better precision. In order to ensure that the solution is detected, one has to choose a large value of N, say $N = 100$. Also, to reduce the number of cells which satisfy the criteria, but do not contain the solution, we also test for the zeroes of $(O+G)(\omega,\gamma)$ and $(O-G)(\omega,\gamma)$ in addition to the zeros of $O(\omega,\gamma)$ and $G(\omega,\gamma)$. Also, we choose the maximum and minimum values for the domains for ω,γ by ensuring that these limits contain ω,γ calculated from the results of the corresponding simulation.

The solver for linear Landau damping provides us with a precise value for the angular frequency ω, and consequently the real phase velocity $v_\phi = \omega/k$ and damping rate γ for arbitrary $|\gamma/\omega|$. Also, this solver works for an arbitrary values of k, q and hence an arbitrary initial q-distribution f_{q_0}. This helps us benchmark the Vlasov-Poisson solver for linear Landau damping, for arbitrary values of ω, k, for arbitrary q-values. From here on, we refer to solutions obtained from numerically solving the dispersion relation (3.5) as 'analytically' obtained value.

We now benchmark the nonlinear Vlasov-Poisson solver using the 'analytical' solver for a short period of $t = 200$. For this purpose, we run our simulations for values of q from 0.5 to 1.2. We also have used the analytical solver to compute the values of ω and γ for these runs. We calculate the values of ω and γ from the data obtained from the simulations. ω is calculated from the data for E_1 till $t = 200$ and γ is calculated till the

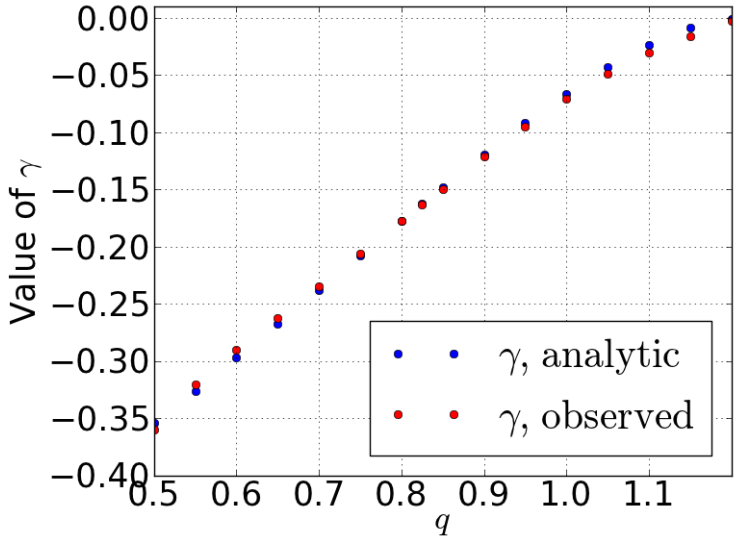

Figure 3.1: Comparison of the 'analytically' obtained and simulated values of the damping rate γ varying with q ($k = 0.4, \alpha = 0.05$).

linear phase of Landau damping which lasts till about $t = 25$. Since nonlinear behavior sets in soon after $t \sim 25$, measuring ω till $t = 200$ takes into account the nonlinear oscillations also. This leads to a small discrepancy in ω values between the 'analytically' obtained and the observed results. Even so, the observed values are within 3% of the analytical value. The plot for comparison of analytically obtained and observed values of γ can be found in the Fig. 3.1. We can see that the analytically obtained and values of γ obtained during the linear phase of the nonlinear solution match well, demonstrating the correctness of the numerical solver. Also, for $q > 1.2$, the damping rate γ is analytically obtained to be zero, and the corresponding value of ω is such that $v_\phi > v_{\text{cutoff}}$, and hence is unphysical. Also, for $q = 1.2$, even though $v_\phi < v_{\text{cutoff}}$, the phase velocity lies very close to the cutoff velocity. Therefore, the PBC applied on the velocity domain might result in unphysical effects. Hence, we do not consider cases for $q \geq 1.2$. However, for $q = 1.15$, when changing k from 0.4 to 1.2, for $\alpha = 0.05$, the value of $v_\phi = \omega/k$ decreases to lie within the 'bulk' of the q-distribution, which enables us to calculate γ accurately . However, on increasing k, the value of the damping rate γ also increases. This can be seen in Fig. 3.2 for the numerically obtained values of γ varying with q for different k within the linear domain. One can see that the values of $|\gamma|$ for a higher k are larger than those with a lower k. Thus, in general for any value of q, we find that increasing k results in a higher damping rate. This observation has great impact in formation of nonlinear structures. We shall come back to this point later.

As discussed earlier, we have performed an additional benchmark. For example, for sufficiently lower values of k where $|\gamma/\omega| \ll 1$, we have compared our analytical solver with the solution given by Valentini and D'Agosta. We find that, for $q = 0.95$ and $k = 0.01$, the analytically obtained value of ω from our dispersion relation solver matches

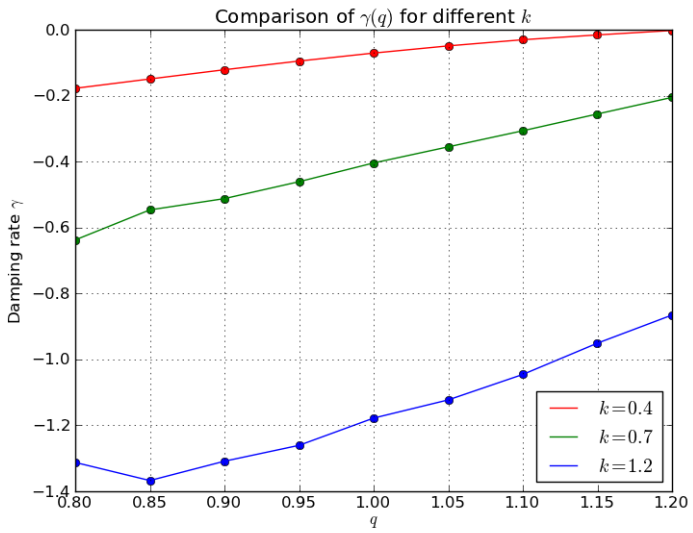

Figure 3.2: Plot of damping rate γ as a function of q for values of $k = 0.4, 0.7, 1.2$. One can see that as k increases, the values of γ are higher than those for a lower k.

with the result from Valentini and D'Agosta's to 0.016%. Also, among all simulations reported in the present work, the maximum change in energy is observed to be within 0.012%. Now that we are confident about the accuracy of the solver, we proceed to extend the simulations into the long-time regime.

3.2 Nonlinear Landau damping

3.2.1 Case $q = 1$

Let us consider the simulation for the $q = 1$ case, which is the normalized Maxwellian. For the value of $k = 0.4$, this simulation corresponds to Manfredi's case[7]. Also, we choose N_x and N_v in such a manner that there is sufficient resolution in x and v. Also, a large value of N_v is needed to push the recurrence as far away as possible, which occurs at $T_R = L/\Delta v$. We now proceed to show that we have been able to replicate Manfredi's results with our solver.

Following Manfredi, the gridsize is set to $N_x = 512, N_v = 4000$, which has been shown to be quite accurate for long-time simulations[7]. The choice of parameter results in the recurrence time $T_R \sim 5326$. Also, in the past, BGK structures were seen to be sustained till $t = 1600$[7]. We have extended Manfredi's run till $t = 5000$ and find the electric field structure to sustain. This can be seen in Fig. 3.3, where we have plotted the amplitude of the fundamental harmonic of the electric field, denoted by E_1, evolving with time. Since we have only perturbed with only one Fourier mode, the fundamental harmonic E_1 would represent how this mode evolves with time. Similarly, the evolution of higher harmonics is a representation of how quickly energy is dissipated among various modes.

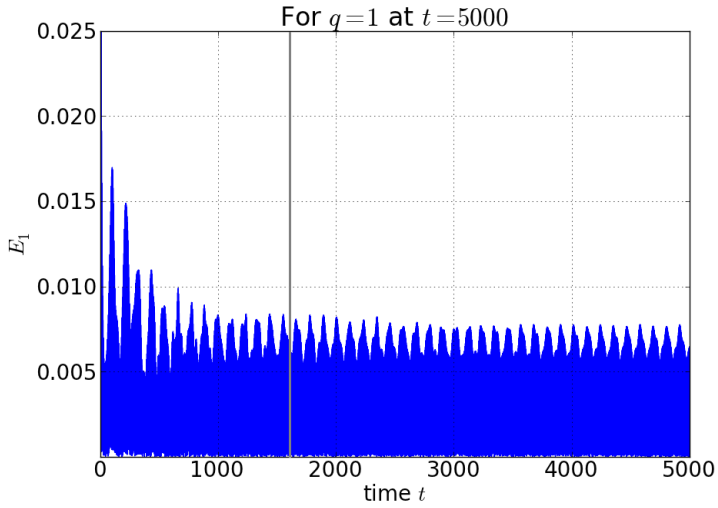

Figure 3.3: A run corresponding to Run I of Manfredi [7], who had shown the oscillations to continue till $t = 1600$. We extended the run till $t = 5000$. The vertical grey line indicates the duration of Manfredi's simulations. Notice the continuation of the oscillations.

This has been thoroughly benchmarked in the appendix. (The vertical grey line indicates the duration of Manfredi's simulations.)

In the phase-space, a vortex structure is created by particle dynamics during nonlinear evolution. The resonant region is the region in phase-space where phase velocity v_ϕ matches with the particle velocity facilitating resonant exchange of energy between the wave and the particles leading to trapping-detrapping dynamics. Therefore, we look for the vortex in the distribution function f around the phase velocity $v_\phi = \omega/k$ obtained by solving Eqns.(3.6) and (3.7) (around which particles exchange energy with the wave). In this case, the analytical value of $\omega = 1.28506$ for $k = 0.4$, and hence $v_\phi = \omega/k = 1.28506/0.4 \approx 3.21$. The plot for phase-space vortex is a frame moving with velocity $v = 3.21$, shown in Fig.3.4(a) at time $t = 5000$.

One can see from this figure that there is a phase-space vortex in the distribution function. This, and the figure for E_1, implies that there is a prominent potential well formed, and particles keep getting trapped and detrapped to sustain the steady-state potential well. We can see that this process continues till $t = 5000$, far beyond Manfredi's run of $t = 1600$, demonstrating clearly that such trapping oscillations are sustained for long-time. We now would like to check the velocity distribution function $\hat{f}(v)$ for non-monotonicity generated by nonlinear Landau damping, at $t = 5000$. The velocity distribution function is given by:

$$\hat{f}(v,t) = \frac{\int_0^L f(x,v,t)dx}{\int_{-v_{\max}}^{v_{\max}} \int_0^L f(x,v,t)dxdv}. \tag{3.9}$$

In 3.4(b), we show the resultant nonmonotonous steady-state velocity distribution func-

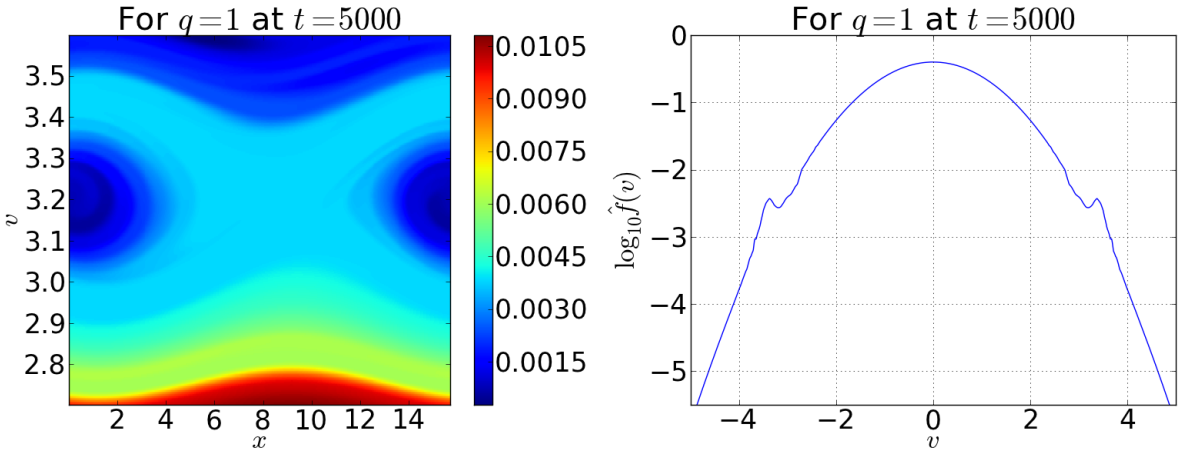

(a) Plot of distribution function $f(x, v)$

(b) Plot of $\log_{10} \hat{f}(v)$.

Figure 3.4: For q=1, at $t = 5000$, the phase-space vortex can be seen around at $v = 3.21$.

tion. Existence of phase-space vortex in the frame moving with the phase velocity $v_\phi = \pm 3.21$ is clearly demonstrated. We can also infer that the non-monotonicity of $\log_{10} \hat{f}(v)$ plot can be used to assess the final form of a steady-state travelling wave solution.

In the original work, BGK solutions are constructed by "arranging" number of particles trapped (and untrapped) in potential-energy troughs (and crests), leading to vortices in phase-space and nonmonotonicity in $f(v)$[5]. In our simulations, we observe phase-space vortex structures and its sustenance throughout the time of the simulation. Moreover, this BGK-like structure moves with a constant velocity which accurately matches with the phase-velocity analytically obtained. We, hereon, refer to such solutions as 'BGK structures,' which we believe, based on the above said arguments, are close to analytically constructed steady BGK modes.

We study the numerical entropy for $q = 1$. The numerical entropy $S(t)$ is computed by:

$$S(t) = \int_0^L \int_{-v_{\max}}^{+v_{\max}} f(x, v, t) \log f(x, v, t) \; dv \; dx \tag{3.10}$$

We plot relative entropy, defined as $S_{rel} = (S(t) - S(0))/S(0)$, with time. This can be seen in Fig.3.5.

Because of the numerical scheme, the entropy monotonically increases with time. The numerical entropy is a measure of the information "lost" from the simulation. As is well known, the evolving distribution function exhibits filamentation which generates a small-scale structure in phase-space. The numerical entropy saturates when the small-scale structures generated are dissipated when this filamentation reaches the gridsize[29], rendering a numerical steady-state. (Nevertheless, the growth of entropy is small, signifying that the information loss is small). Obviously, one can see that the entropy has saturated at around $t = 1500$. It has been shown in the past that such dissipation of small-scale

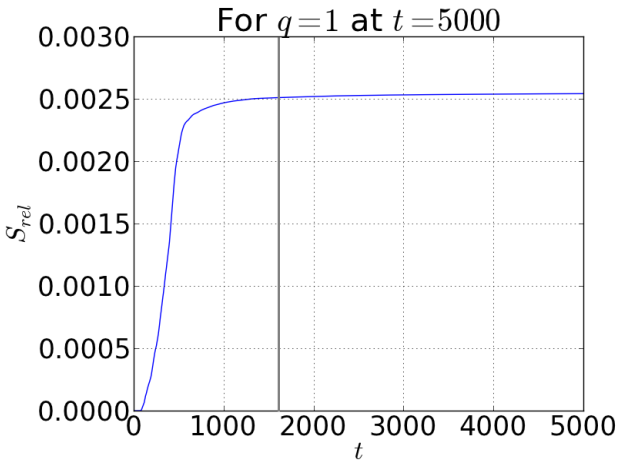

Figure 3.5: Plot of relative entropy S_{rel} with time. The vertical line represents the duration of Manfredi's simulation.

structures do not affect the large-scale solution obtained[29, 7]. Also, one can notice that the numerical entropy saturates nearly at the same time the value of E_1 reaches steady-state. Saturation of this numerical entropy in time may be used as a diagnosis to determine the numerical steady-state of the solution in the nonlinear phase.

To summarize $q = 1$ results, we observe that the electric field E_1 initially undergoes few oscillations and then settles to oscillate around a non-zero value. On inspection of the phase-space, we find that phase-space vortex which leads to nonmonotonicity in the velocity distribution function. Also, we find that the phase-space vortex moves with a constant velocity for the entire simulation. Also, the numerical entropy (which we use as a measure of whether the system has attained a numerical steady-state) saturates at a constant value. Thus, we can infer that this non-zero electric field structure, in a neutral Vlasov plasma, moving with a constant phase velocity, is a BGK-like solution which we call a 'BGK structure.'

One can find the complete benchmark process, including other diagnostics, for nonlinear Landau damping for Maxwellians in Sec. B.3. Now that we have observed nonlinear Landau damping on $q = 1$ distribution leading to BGK structure, and reproduced Manfredi's results in the process [7], we wish to study the long-time fate of similar perturbation on $q \neq 1$ distributions. For this purpose, we perform runs for two different sets of q values:

3.2.2 Case $q < 1$

In case of $q < 1$, the distribution functions, as compared to the Maxwellian, exhibit a lower peak and a longer tail. Therefore, we choose the following parameters in the solver to accommodate for these changes.

We give runs for $0.5 \leq q < 1$ varied in steps of 0.05, and will be referred to as 'Set I.' For Set I, we choose $v_{\max} = 12.5$, $N_v = 8000$, $N_x = 512$, and keep rest of the initial conditions same as Manfredi's. For these runs, the recurrence time $T_R \sim 5026$ and, thus,

we choose to run the simulation till $t = 2000$. Also, it is important to note that, for any q-distribution in this set, we observe that the phase velocity $v_\phi = \omega/k$ lies well within the bulk of the distribution, far from $v_{\max}$.

Now, similar to the case for $q = 1$, we wish to see the evolution of E_1 with time. The graphs obtained for E_1 are plotted in Fig.3.6. We have not shown graphs for $q < 0.80$ because, for $q \leq 0.80$, E_1 damps and stays damped. Furthermore, with decreasing value of q, the value of $|\gamma|$ increases and, hence, the time in which the system damps decreases. Hence, the lesser the value of q, the faster it damps. Also, the behaviour shown by the system is maintained even when the simulation is extended to run till $t = 3000$.

We can see that the oscillations cease to exist somewhere in the interval $q \in [0.80, 0.85]$. We ran the code for an intermediate value of $q = 0.825$. We observe that for this case too the oscillations in E_1 arise, albeit at later time. We, in fact, observe this trend in those values of q for which BGK structure arises, that as q decreases, and $|\gamma|$ increases, the time taken for the oscillations to arise increases.

Now again, we wish to see the plots for relative entropy with time S_{rel}. In this case, entropy $S(t)$ is defined as[15]:

$$S_q(t) = \int_0^L \int_{-v_{\max}}^{+v_{\max}} f(x,v,t) \left(\frac{1 - f(x,v,t)^{q-1}}{q-1} \right) \, dv \, dx. \tag{3.11}$$

which is the same as q-nonextensive entropy. Note that for the limit $q = 1$, Eq. (3.11) reduces to Eq. (3.10). The plots for relative entropy for Set I can be seen in Fig.3.7. For the cases where BGK structures are found, the entropy curves are similar to the curve for $q = 1$. Also, one can notice that smaller the value of q, the later the entropy seems to grow and stabilize. Also, we extended the simulation till $t = 3000$ in order to confirm the formation of a steady-state solution. From the figures for E_1, we conclude that the long-time solution is indeed a BGK structure for $0.85 \leq q \leq 0.95$.

Also, for $q \leq 0.80$, the curves for entropy (not shown) have a different shape, and do not saturate at a fixed value. The phase-space plots of the distribution functions, in the vicinity of v_ϕ, also does not reveal any vortices. For this reason, we believe that within $t = 3000$, cases $q \leq 0.8$ do not lead to phase-space vortices and consequently do not exhibit BGK-like solutions. (In order to verify that the monotonic damping for case $q = 0.8$ is not a numerical phenomenon, we ran the same code with higher resolution in x and v, with $N_x = 2048$, $N_v = 16000$ and $v_{\max} = 25$, keeping rest of the parameters the same. For this run too, the oscillations damp quickly and stay damped. Thus, the lack of formation of a BGK structure is not simply a numerical phenomenon.)

For the case of $q = 0.85$ (which is close to the value of q for which BGK structures do not form), we wish to see the structure of the distribution function. For $q = 0.85$, the analytic value of $\omega = 1.31135$ for $k = 0.4$ and, hence, $v_\phi = \omega/k \sim 3.28$. Thus, we plot the distribution function around v_ϕ. The plot can be seen in Fig.3.8. Even though, for $q = 0.85$, a phase-space vortex is formed in the vicinity of $v = v_\phi$. This structure is better formed for $q = 0.9$, for which the amplitude of E_1 is greater than that of $q = 0.85$ and thus looks 'weak' in the figure, which is similar to the result obtained by Valentini[20]. We can also see that this structure has sustained till $t = 3000$. Thus, from E_1, S_{rel} and the phase-space vortex, we can conclude that the solution is a BGK structure.

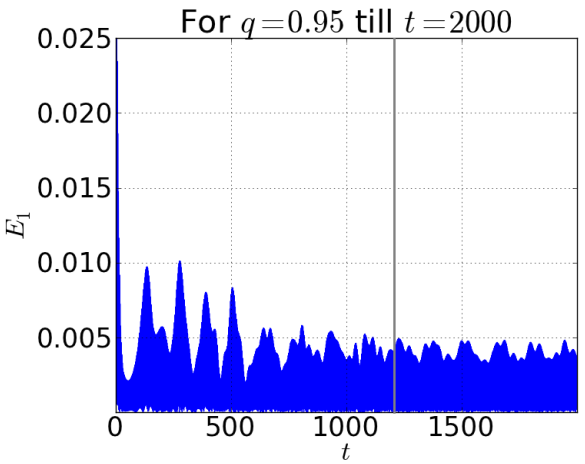

(a) $q = 0.95$

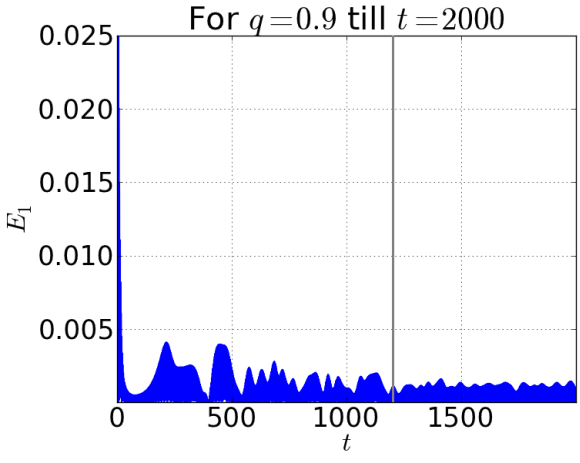

(b) $q = 0.90$

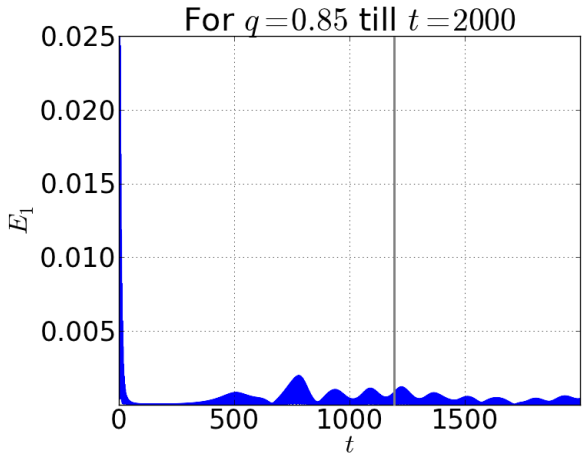

(c) $q = 0.85$

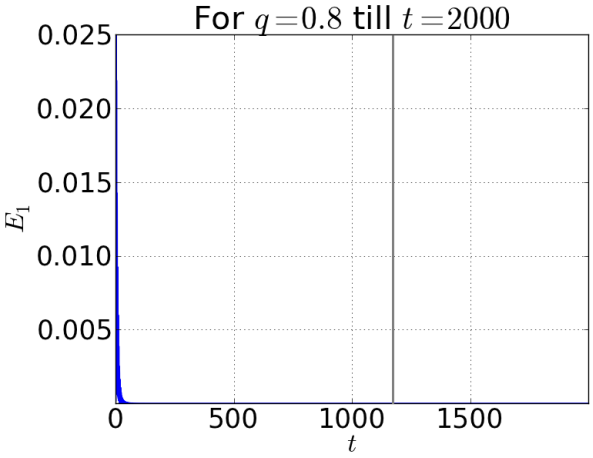

(d) $q = 0.80$

Figure 3.6: Plots for the amplitude of the first harmonic of the electric field E_1 with time for Set I. One can notice that the oscillatory structures are not found for $q \leq 0.80$. Also, as damping rate increases, one can notice that the amplitude of oscillations decreases. This is similar to the result obtained by Valentini[20]. The vertical line represents the time of Valentini's simulations.

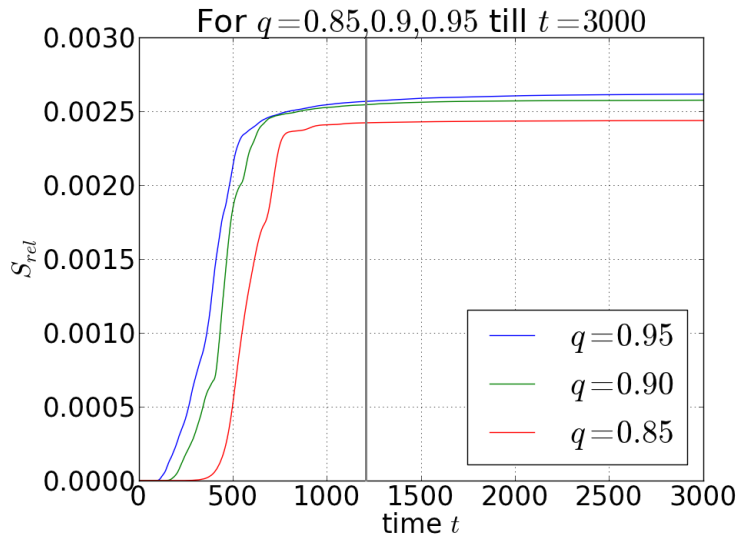

Figure 3.7: Plot of relative entropy S_{rel} with time for $q < 1$ till $t = 3000$. The vertical line represents the time up to which Valentini's simulations were performed.

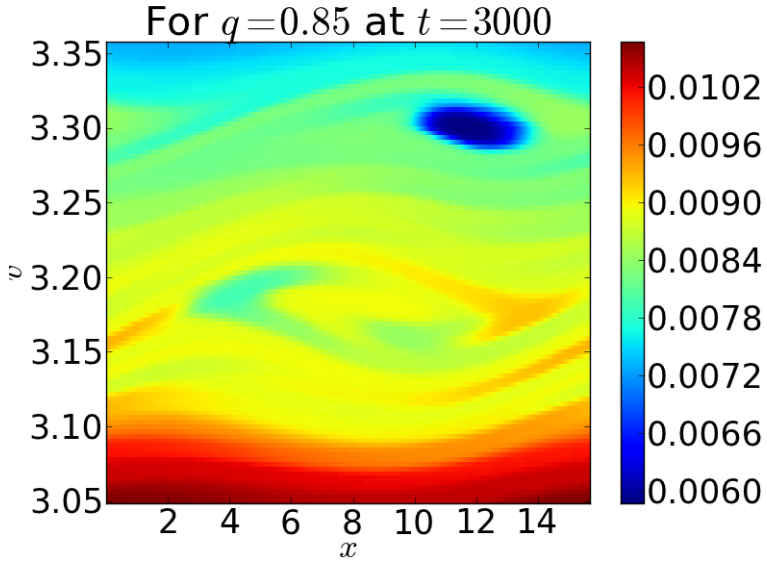

Figure 3.8: Plot of distribution function for the run with $q = 0.85$, around $v_\phi = 3.28$, at $t = 3000$.

Furthermore, in terms of the independent parameters in the simulation, for $k = 0.4, \alpha = 0.05$, the value of $q \sim 0.8$ seems to be the critical q at which the transition of behavior from completely damped to formation of BGK mode occurs. Therefore, one can say that the window for sustaining BGK modes in $q < 1$ is restricted by the damping rate $|\gamma|$ which increases for decreasing q. Thus, below the critical q, the electric field is damped away before a potential well for trapping is formed.

Now, we move on to the next set of runs corresponding to $q > 1$.

3.2.3 Case $q > 1$

We can notice from the velocity distribution function Eq. (3.3) that for $q > 1$, the distribution function exhibits higher peak and a shorter tail. Also, it exhibits a velocity cutoff at $v_{\text{cutoff}} = \sqrt{2/(q-1)}$, beyond which the function becomes unphysical.

Again, similar to Set I, we give runs for $1 < q \leq 1.15$ in steps of 0.05, and refer to this set of runs as 'Set II.' For the Set II, we choose $v_{\max} = v_{\text{cutoff}}$ and keep grid sizes and rest of the initial conditions the same. The minimum value for the recurrence time $T_R \sim 9934$ (as a result of smaller $v_{\max}$).

In this case, the periodic boundary conditions (PBCs) set on the v-domain may affect the simulations if the resonant region is close to the boundaries. Therefore, we consider only those cases for which the resonant region is sufficiently far away from the boundaries. Hence, as mentioned earlier, we don't consider cases $q \geq 1.2$, as $v_{\text{cutoff}} \lesssim v_\phi$ for increasing $q > 1$. Clearly, one can increase the value of k, so as to make the value of $v_\phi = \omega/k$ lie within the 'bulk' of the distribution function. However, as we have observed that increasing k leads to an increase in γ and, therefore, the advantage of having v_ϕ more distant from v_{cutoff} is overshadowed by the field being damped rapidly (Fig.3.2). We shall come back to this point soon.

For the cases $1.05 \leq q \leq 1.15$, we now wish to see the evolution of E_1 with time. These can be seen in the Fig.3.9. One can notice that the oscillations continue at a non-zero amplitude, similar to $q = 1$. Next, we now check $S_{rel}(t)$ to see whether filamentation affects the long-time solutions. This can be seen in Fig.3.10. The shape of entropy curves are different from the earlier cases, which may be because of higher resolution in v domain. One can see that the entropy has not saturated within $t = 1200$. However, it can be clearly seen, for $1.05 \leq q \leq 1.15$, that the relative entropy curves settles to steady-state at a higher value than the other q values, within $t = 3000$.

For $q = 1.15$, we wish to see the distribution function at around $v = v_\phi$. In this case, the analytically obtained $\omega = 1.22917$ and, hence, $v_\phi \sim 3.07$. Thus, we plot the distribution function around v_ϕ at $t \sim 2000$. This can be seen in Fig.3.11. In this case too we can see the phase-space vortex clearly and see the corresponding value for E_1, which resembles the case for $q = 0.95$ and $q = 1$. Thus, this long-time state is also a BGK structure solution.

However, for higher q-values, the decrease in v_ϕ is offset by a competing higher k damping. To keep $v_\phi \ll v_{\text{cutoff}}$, k has to be increased. For this purpose, we perturb with a higher value of k, initialized with $q = 1.30$ distribution. We keep α and the grid sizes same

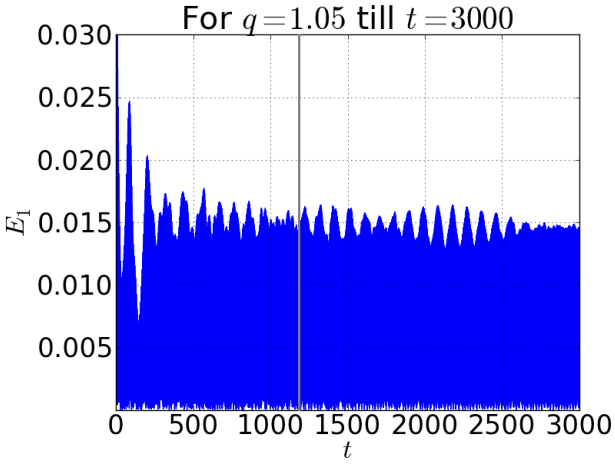

(a) $q = 1.05$

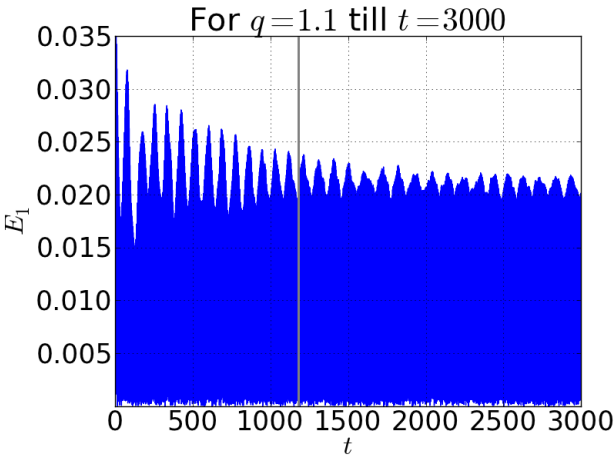

(b) $q = 1.10$

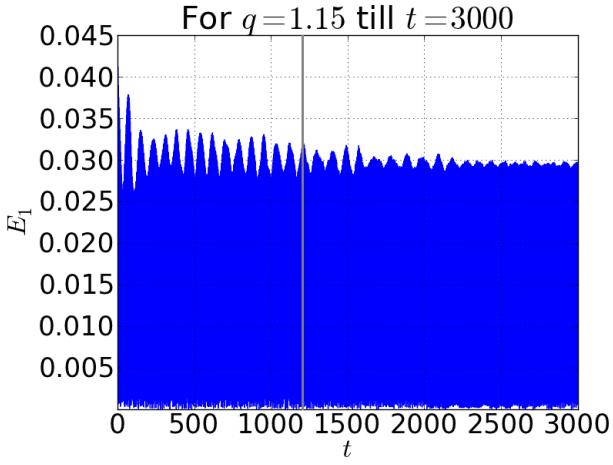

(c) $q = 1.15$

Figure 3.9: Plots for the amplitude of the first harmonic of the electric field E_1 with time. The vertical line represents the time of Valentini's simulations. As we can see, the field has not saturated within this time.

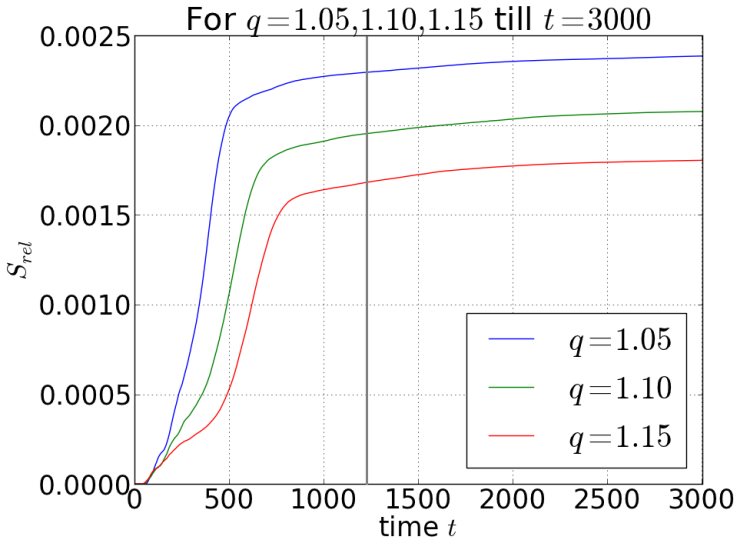

Figure 3.10: Plot of relative entropy S_{rel} with time for $1.05 \leq q \leq 1.15$. It can be seen that the entropy saturates within $t = 3000$. The vertical line represents the time up to which Valentini's simulations were performed.

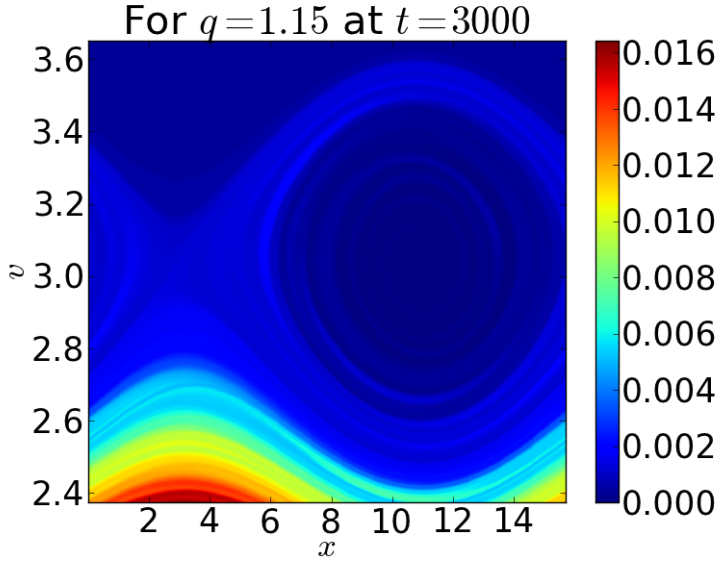

Figure 3.11: Plot of distribution function for the run with $q = 1.15$, around $v_\phi = 3.07$, at $t = 3000$.

as in the earlier cases. Increasing k causes the value of v_ϕ to decrease. We perturb with $k = 0.7, 1.2$, which corresponds to $v_\phi \sim 2.29, 2.07$ respectively, both under $v_{\text{cutoff}} \sim 2.58$. On perturbing with $k = 0.7$, we see oscillations in E_1 (implying a BGK mode solution) and perturbing with $k = 1.2$, we see that E_1 gets damped quickly and stays damped. This occurs because, with increasing k, keeping α constant, as mentioned earlier, the absolute value of γ increases (Fig.3.2), which renders difficult the formation of BGK structures. For Maxwellian plasma, this effect has been observed in the past[29]. Therefore, we may reasonably expect such a transition for any q-distribution which shows BGK structures for some value of α, k. This phenomenon was not considered by Valentini, who states that trapping for $q > 1$ is extremely efficient[20]. We, however, find that the efficiency of trapping decreases with increasing k, eventually leading to monotonic damping at a critical k.

As discussed before, the change in behaviour from trapping to monotonic damping is also known to occur for Maxwellian ($q = 1$). In order to check, we gave runs for $q = 1$ with $k = 0.4 - 1.2$, with the same α, till $t = 2000$. We found that the critical value of k lies between 0.49 and 0.5, between which the behaviour changes from BGK mode formation to exponential damping. For $q = 1$, for this critical value of k, for $\alpha = 0.05$, we find that $\gamma\tau \sim 0.67$. As pointed out empirically by Manfredi, the index $\gamma\tau$ plays a critical role in determining the long-time behaviour of the system. For an initial Maxwellian, it has been previously reported by Manfredi that, there seems to be a critical value of $\gamma\tau \sim 0.5$ around which the behaviour of a system changes[7]. However, Ivanov, Cairns and Robinson have reported a critical $\gamma\tau \sim 1$ for such a change[10].

Valentini has subsequently studied the dependence of critical value of τ on q for q-distributions.[20]. To understand the effect of perturbation amplitude better, we considered the limiting case of $q = 0.8$, for which BGK structures were not found. On increasing the value of α from 0.05 to 0.1, we find BGK structures start to form again. It is reasonable to expect that the resurgence of formation of BGK structures occurs for any value of q. Furthermore, for another value of $k = 0.5$, we have studied the variation in the value of $\gamma\tau$ for different values of q in the linear phase of Landau damping. We observe that for $q \leq 0.9$, $\gamma\tau > 1$. Since we have already seen that $k = 0.5, q = 1$ represents a critical value of the change in behaviour and that the damping rate increases with decreasing q, we can reasonably conclude that trapping is not observed for those q-values for which $\gamma\tau > 1$. It is also reasonable to generalize that damping at k values higher than a critical value occurs for any q-distribution. Especially for q-distributions with $q > 1$, these phenomena severely restrict the window in α, k within which one can observe BGK modes.

Now, we wish to compare the results obtained from the runs corresponding to $0.85 \leq q \leq 1.15$, for which a BGK mode solutions are formed. To do so, we construct a semi-log plot for the velocity distribution function $\hat{f}(v)$ to see where the phase-space vortex is. This can be seen in Fig.3.12. For these values of q, from Fig.3.12, one can notice that distinct non-monotonicity is observed the vicinity of $v = \pm v_\phi$. Also, for the case of $q = 0.85$, for which the field E_1 is weak, we can see that this structure looks rather diminished. Also, this nonmonotonicity becomes more prominent and visible with increasing q. Thus,

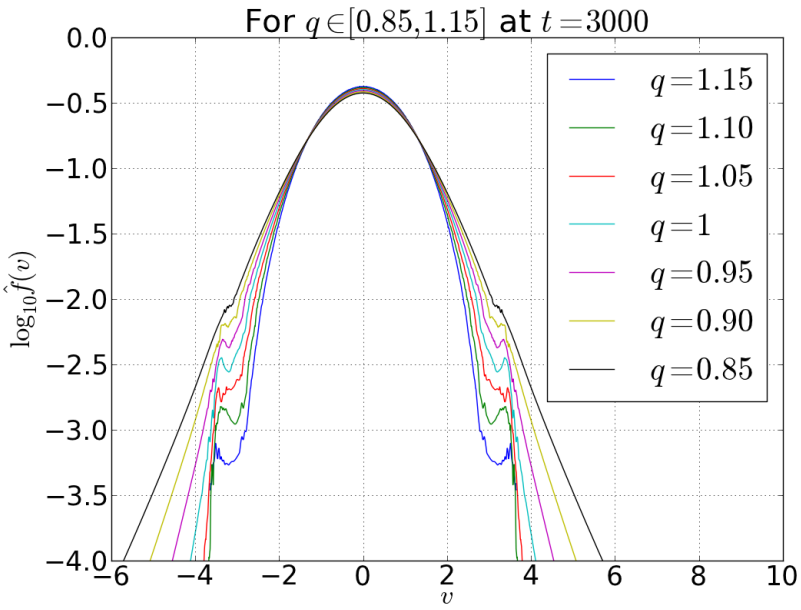

Figure 3.12: Plot of velocity distribution function $\log_{10} \hat{f}(v)$ at $t = 2000$ comparing cases with $0.85 \leq q \leq 1.15$.

one can say that BGK structures, for a given perturbation, can occur beyond the critical value of q as long as v_{cutoff} is greater than and sufficiently far away from v_ϕ. Also, as q increases higher damping rate at larger k values severely limits the window in q for the formation of steady-state BGK structures.

Chapter 4

Summary

The work done in development of the solver can be summarized as follows:

1. We developed and benchmarked a Vlasov-Poisson solver based on the piecewise-parabolic method(PPM) advection solver. The comprehensive benchmark of the individual components and the assembled solver itself can be found in the appendices.

2. We developed an analytical solver which solves for the angular frequency ω and damping rate γ from the numerical solution of the Vlasov-Maxwell system. We find that the solution obtained from this solver independently agreed with the solution obtained from the numerical solver. This is the key benchmark that gives us confidence on the accuracy of the solver.

3. We performed long-time simulations of known results of nonlinear Landau damping, i.e. Manfredi's and Valentini's simulations. We find that our solver is in very close agreement with the results previously obtained by them. This conclusively showed that our solver is robust for long-time simulations.

Using this solver, we study nonlinear Landau damping, for times up to $t = 3000\omega_p^{-1}$ on q-nonextensive velocity distributions for a window around $q = 1$. The results of the simulation can be summarized in the following points:

1. For a given perturbation amplitude α and perturbation wavenumber k, we demonstrate existence of a window in q where BGK structures are shown to sustain for very long times. For example, for $k = 0.4, \alpha = 0.05$, there is a window around $q = 1$ for which we can see BGK structures. As q decreases below $q = 1$, the electric field damps quicker. After a critical value of q, damping renders the existence of BGK structures difficult and, hence, the electric field is found to monotonically damp away. Therefore, for $q < 1$, the formation of BGK modes is limited by the increasing damping rate γ with decreasing q and, in the process, confirmed Valentini's observation up to $t = 3000\omega_p^{-1}$.

2. As q increases beyond $q = 1$, the perturbation causes the phase velocity to come closer to the velocity cutoff of the $q > 1$ distribution. Because of this, there exists an upper limit on q below which we find BGK structures. Beyond this limit, the perturbation does not cause Landau damping (hence rendering such a situation unphysical). To remedy this, we increased the value of k, which causes the phase velocity to lie within the bulk of the distribution. But this also causes the damping rate to increase and, thus, a critical value of k exists beyond which BGK structures cannot be found. Thus, in the $q > 1$ domain, whenever nonlinear Landau damping occurs, the formation of BGK structures is limited by an upper limit on k. This had not been observed previously and leads to a severe restriction on the window for $q > 1$ within which trapping occurs.

3. We have shown, using high-resolution Vlasov-Poisson solver for long-times up to $t = 3000\omega_p^{-1}$ that the formation of BGK structures seems to depend critically on the independent parameters q, k, α. Additionally, there also seems to exist a lower limit to the perturbation amplitude α below which BGK-structures are not observed. Further, such a limit seems to exist independently for any q-distribution with arbitrary initial k. Also, the parameter $\gamma\tau$, which reflects changes in both α and k, seems to play an important role in determining the behaviour of nonlinear Landau damping.

4.1 Publication

Our work has been published published in *Physics of Plasmas*[33]. Also, it has been presented at *International Conference On Complex Processes In Plasmas And Nonlinear Dynamical Systems (ICCPPNDS-2012)* held at Institute for Plasma Research (IPR), Gandhinagar, India.

4.2 Future Work

We list the future work with our solver:

- Colella and Sekora have published a paper on a 6th order approximation to correct for the first order error at extrema[34]. We wish to implement this correction, as it only applies at the extrema. Therefore, it may not alter the performance of the code.

- GPU Parallelization of the algorithm, so as to speed up the solver. In this process, we may replace the Poisson solver with an algorithm to solve for the Ampere/Maxwell equation[35], so as to ease parallelization.

- Addition the ion component to the solver, in order to solve for phenomena in which ion interaction becomes significant.

- Study of ion-acoustic turbulence[36] and anomalous resistivity[37, 38, 39, 40] for 1D plasmas. The study of anomalous resistivity is important as it may be an indicator of magnetic reconnection[41] in plasmas.

- Study of formation of jets in collisionless 1D relativistic and non-relativistic plasmas[42]. This will require only minor modifications to the present solver. However, high velocity jets can be formed out of plasmas with relatively low temperatures. Therefore, we need a high resolution for this purpose which warrants parallelization of the code before attempting this problem.

- Study of sheath formation around conducting walls using kinetic simulations[43, 44, 45]. This problem is special in the sense that one of the walls has to be made conducting. So, instead of the finite-volume-method like simulation used in this work, we have to modify the solver to represent the complete system in the x-domain. We also need to be able to account for different boundary conditions as per the need.

- Modification of the solver so as to be able to account for sources and sinks. This would help in studying Berk-Breizman phenomenology[47].

- Study of trapping of particles in the BGK mode corresponding to the Bump-on-Tail instability[46] for different initial distributions.

- Furthering the study of nonlinear Landau damping for different types of initial perturbations.

4.3 Software

All the codes were written in `FORTRAN90`. For Fourier transforms required to solve the Poisson equation, `FFTW 3.2` is used[48]. All the graphs were plotted in `Python 2.7.3`, using `IPython 0.12.1`[49] running `Matplotlib 1.1.0`[50]. The python packages used were bundled in the Enthought Python Suite (ver. 7.3-1) running under an academic license.

Bibliography

[1] L. Landau, J. Phys. USSR **10**, 25 (1946), English translation reproduced in '*Collected papers of L.D. Landau*', edited and with an introduction by D. ter Haar, Pergamon Press, 1965, pp. 445–460.

[2] F. F. Chen, *Introduction to Plasma Physics and Controlled Fusion (2E.)*, Vol. 1, Plenum Press, Sec. 7.2 (Chap 7), (1984).

[3] J. H. Malmberg, C. B. Wharton, R. W. Gould, and T. M. O'Neil, Physics Review Letters **20**, 95 (1968).

[4] T. O'Neil, Physics of Fluids **8**, 2255 (1965).

[5] I. B. Bernstein, J. M. Greene, and M. D. Kruskal, Physical Review **108**, 546 (1957).

[6] M. B. Isichenko, Physical Review Letters **78**, 2369 (1997).

[7] G. Manfredi, Physical Review Letters **79**, 2815 (1997).

[8] C. Lancellotti and J. Dorning, Physical Review Letters **80**, 5236-5236 (1998)

[9] M. C. Firpo and Y. Elskens, Physical Review Letters **84**, 3318 (2000).

[10] A. Ivanov, I. Cairns, and P. Robinson, Physics of Plasmas **11**, 4649 (2004).

[11] J. Barré and Y. Y. Yamaguchi, Physical Review E **79**, 036208 (2009).

[12] M. Ouazene and R. Annou, Physics of Plasmas **18**, 114502 (2011)

[13] M. V. Goldman, D. L. Newman, and A. Mangeney, Physical Review Letters **99**, 145002 (2007)

[14] H. Schamel, Physics of Plasmas **19**, 020501 (2012)

[15] C. Tsallis, Journal of Statistical Physics **52**, 479 (1988).

[16] R. Silva Jr, A. R. Plastino, and J. A. S. Lima, Physics Letters A **249**, 401 (1998).

[17] M. Tribeche, L. Djebarni, and R. Amour, Physics of Plasmas **17**, 042114 (2010).

[18] A. Lavagno and P. Quarati, Nuclear Physics B - Proceedings Supplements **87**, 209 (2000), *Proceedings of the Sixth International Workshop on Topics in Astroparticle and Underground Physics*.

[19] A. Lavagno, G. Kaniadakis, M. Rego-Monteiro, P. Quarati, and C. Tsallis, Astrophysical Letters and Communications **35**, 449 (1998).

[20] F. Valentini, Physics of Plasmas **12**, 072106 (2005).

[21] C. Z. Cheng and G. Knorr, Journal of Computational Physics **22**, 330 (1976).

[22] T. Arber and R. Vann, Journal of Computational Physics **180**, 339 (2002).

[23] E. Fijalkow, Computer Physics Communications **116**, 319 (1999).

[24] P. Colella and P. R. Woodward, Journal of Computational Physics **54**, 174 (1984).

[25] J. P. Boris and D. L. Book, Journal of Computational Physics **11**, 38 (1973).

[26] A. Ghizzo, B. Izrar, P. Bertrand, E. Fijalkow, M. R. Feix et al. Physics of Fluids **31**, 72 (1988).

[27] R. Vann, *Characterisation of fully nonlinear Berk-Breizman phenomenonology*, PhD thesis, University of Warwick, 2002.

[28] F. Valentini and R. D'Agosta, Physics of Plasmas **14**, 092111 (2007).

[29] M. R. Feix, P. Bertrand, and A. Ghizzo, Advances in Kinetic Theory and Computing, edited by B. Perthame (World Scientific, Singapore), 45-81 (1994).

[30] G. Strang, SIAM Journal of Numerical Analysis **5(3)**, **506** (1968).

[31] R. W. Hockney and J. W. Eastwood, *Computer Simulation Using Particles*, Bristol,Hilger, Section 6-5-2, **205**, (1988).

[32] K. E. Atkinson, *An Introduction to Numerical Analysis* (2E.), Section 5.1-5.4 (Chap. 5), John Wiley & Sons, (1989)

[33] M. Raghunathan and R. Ganesh, Physics of Plasmas **20**, 032106 (2013)

[34] P. Colella and M. D. Sekora, Journal of Computational Physics **227**, 7069 (2008).

[35] Richard B. Horne and Mervyn P. Freeman, Journal of Computational Physics **171**, 182 (2001)

[36] N. V. Elkina and J. Buchner, Journal of Computational Physics **213**, 862 (2006)

[37] J. Büchner, *Advanced Methods for Space Simulations*, edited by H. Usui and Y. Omura, pp. 2346 (2007).

[38] P. Petkaki, C. E. J. Watt, R. B. Horne and M. P. Freeman, Journal of Geophysical Research **108**, A12 1442 (2003).

[39] P. Petkaki, M. P. Freeman, T. Kirk, C. E. J. Watt and R. B. Horne, Journal of Geophysical Research **111**, A01205 (2006)

[40] P. Petkaki and M. P. Freeman, The Astrophysical Journal **686**, 686 (2008)

[41] J. Büchner, Space Science Reviews **124**, 345 (2006).

[42] N. J. Sircombe, T. D. Arber, and R. O. Dendy, Physics of Plasmas **12**, 012303 (2005).

[43] Monojoy Goswami and H. Ramachandran, Physics of Plasmas **6**, 4522 (1999).

[44] Magdi Shoucri, Japanese Journal of Applied Physics **46**, 5A 3045, (2007).

[45] M. Shoucri, H. Gerhauser, and K. H. Finken, Physics of Plasmas **16**, 103506 (2009)

[46] N. J. Balmforth, Communications in Nonlinear Science and Numerical Simulation **17**, 1989 (2012)

[47] R. G. L. Vann, R. O. Dendy, G. Rowlands, T. D. Arber, and N. d'Ambrumenil, Physics of Plasmas **10**, 623 (2003).

[48] M. Frigo and S. G. Johnson, Proceedings of the IEEE **93**, 216 (2005), Special issue on "Program Generation, Optimization, and Platform Adaptation".

[49] F. Prez, B. E. Granger, Computing in Science and Engineering, **9(3)**, 21 (2007)

[50] J. D. Hunter, Computing in Science and Engineering, **9(3)**, 90 (2007)

Appendix A

Benchmarking the PPM Advection Solver and Fourier Transform based Poisson Solver

We need to benchmark the components of the Vlasov-Poisson solver in order to characterize their accuracy and limitations. This might help understand the behaviour of the Vlasov-Poisson solver later. For these benchmarks, we choose $L = 2\pi$, $N = 1000$, and therefore $\Delta x = \frac{2\pi}{1000}$. We apply periodic boundary conditions on the function such that $a_{N+l} = a_l$.

A.1 PPM Advection Solver

For the purposes of the benchmark, we have chosen $u = 0.1$, and then Δt is decided by the CFL condition. We perform advection for the following three cases:

1. Propagation of a periodic sine wave, to study the accuracy of the advection. For this case, we set the CFL number $k = 0.99$ and $k = 1$ in order to establish a pattern to the propagation of errors..

2. A sharp Gaussian, because this would correspond to the physical cases that we would study later.

3. A square wave, to demonstrate the discontinuity detection algorithm.

Initially, all of the three benchmarks are performed for two CFL numbers $k = 0.99$ and $k = 1$. For these values, we study the dependence of the growth of error on the number of advections n. Then, for the first benchmark, we perform a sweep from $k = -1$ to $k = 1$ in order to study the variation of error with k. The timestep is chosen by the rule:

$$\Delta t = k\frac{dx}{u} \tag{A.1}$$

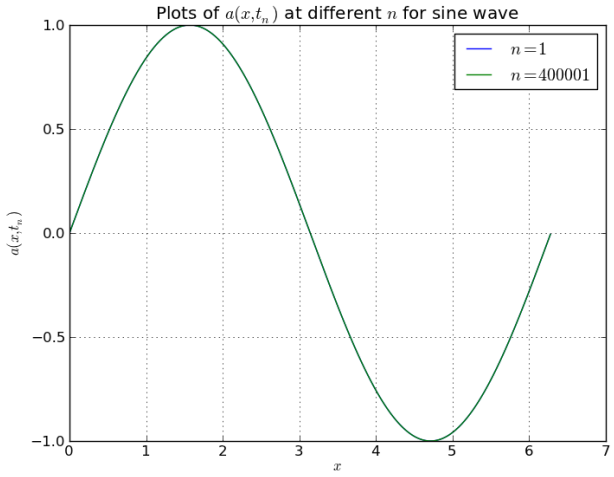

(a) Plot of Waveform

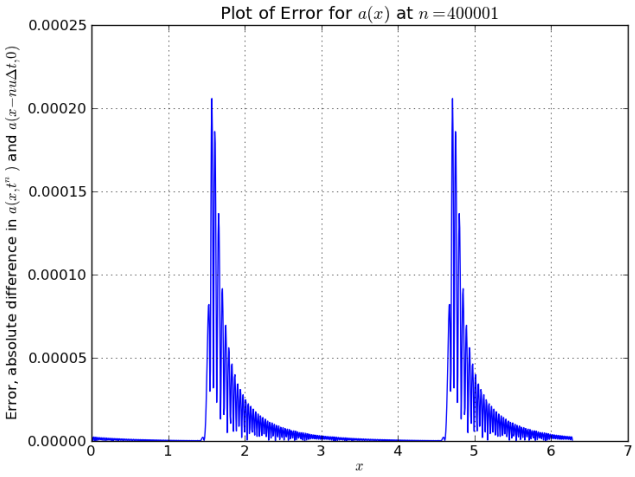

(b) Plot of Error in Waveform

Figure A.1: Plots ($k = 0.99$) of the Waveform at the beginning and the end of the advection, and plot of the error in the Waveform at the end of the simulation.

where k is the CFL number. We give runs of up to timesteps $n = 400000$. Furthermore, it would be interesting to see the results for $k = 1$, as it represents the special case when advection in time of Δt is equivalent to setting $a(x, t + \Delta t) \leftarrow a(x - \Delta x, t)$.

A.1.1 Initial Sine Wave

The initial wave profile is:

$$a(x, 0) = \sin x, \ \ 0 \leq x < 2\pi \tag{A.2}$$

We calculate the error by:

$$\delta a(x, n) = |a(x, n\Delta t) - \sin(x - un\Delta t)| \tag{A.3}$$

where $a(x, n\Delta t)$ represents the advected waveform after the n^{th} timestep. The plots for $k = 0.99$ are shown in figure (A.1). One can see from the figure (a) how there is no noticeable difference between the initial and the final waveform. They overlap because the value of $u\Delta t$ is a multiple of $N\Delta x$. Also, one can notice from (b) that the error is indeed first order $O(\Delta x)$ near the extrema and the error falls off away from the extrema. Now, for the special case of $k = 1$ where advection of one time-step is equivalent to shifting one grid-point to the right, we have the plots in figure (A.2). One can see from (a) how, again there is no noticeable difference in the initial and final waveforms. Also, one can see how, for this special case, the order of error is very low ($O(10^{-13})$)as compared to $k < 1$. This is the direct consequence of the advection being equivalent to a shift in one gridstep.

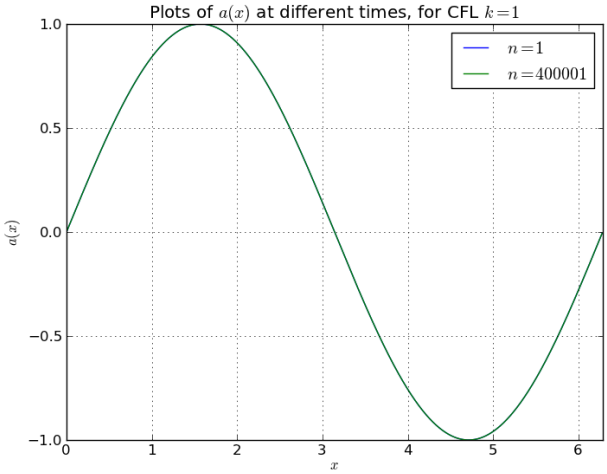

(a) Plot of Waveform

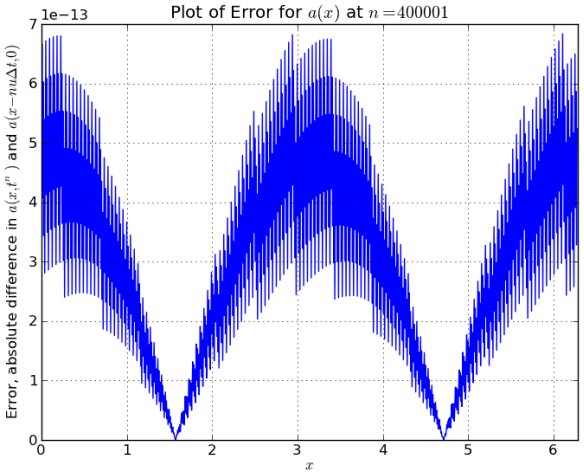

(b) Plot of Error in Waveform

Figure A.2: Plots ($k = 1$) of the Waveform at the beginning and the end of the advection, and plot of the error in the Waveform at the end of the simulation

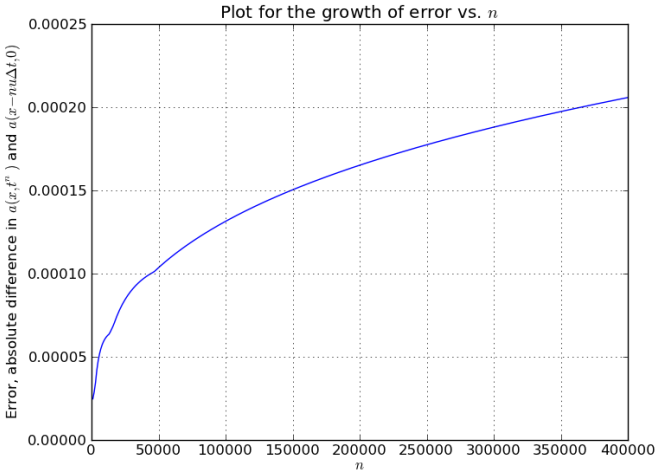

(a) Growth in error with n for $k = 0.99$

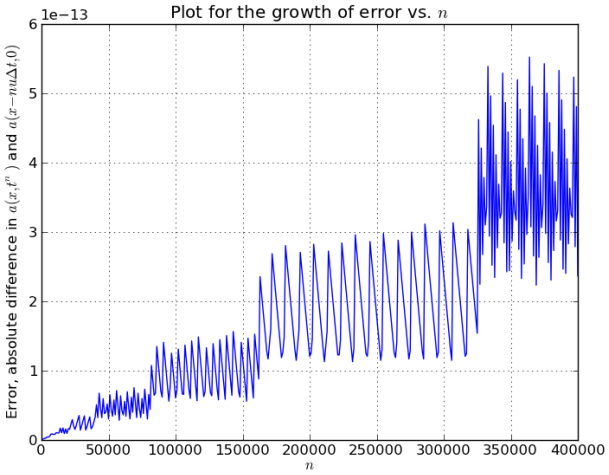

(b) Growth in error with n for $k = 1$

Figure A.3: Plots for the maximum error, $\max(\delta a(x, n))$, defined by (A.3), plotted vs. n for $k = 0.99$ and $k = 1$, up to $n = 400000$

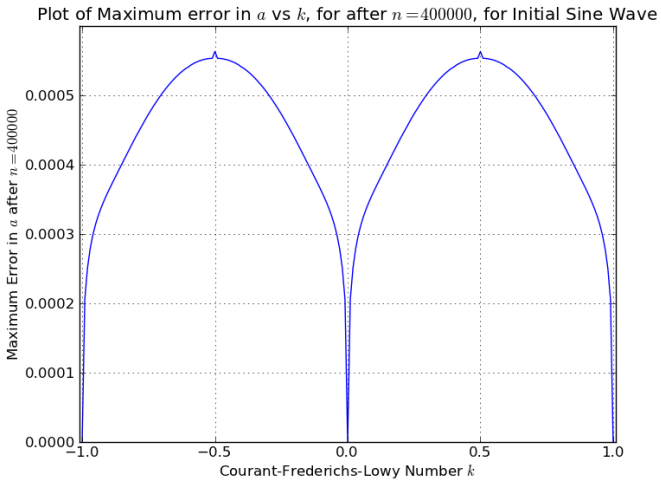

Figure A.4: Plot, for $k \in [-1, 1]$, of the error for initial sine wave, at the end of the advection at $n = 400001$.

It would be interesting to see for both values of k here, how the error grows with progress in time. The plots for those are in figure (A.3). One can see how, for $k = 0.99$ the error keeps increasing, but stays within the order of $O(\Delta x)$, and how for $k = 1$, the error remains in the order of 10^{-13}, and doesn't grow past that order.

Also, it would be interesting to see how the error depends on the value of the CFL number. For this, we apply advection for $n = 400000$ timesteps, and check the error in $a(x, t_{400001})$. We vary the CFL number in the interval $[-1, 1]$, and plot the error thus obtained. Negative CFL numbers represent a negative value for the advection velocity. The reason for benchmarking with negative CFL numbers is that the PPM advection solver applies slightly different expressions for advection for negative and positive values of advection velocities.

One can see from the plot (Fig. A.4) that error is virtually zero for $k = -1, 0, 1$, which is ascribed to the reason mentioned earlier. Also, it can be noticed that the error is symmetric around the $y-$ axis, and also, the errors for positive k are symmetric around $k = 0.5$, and the negative k around $k = -0.5$. Also, the errors peak at $k = \pm 0.5$, irrespective of the actual time $n\Delta t$ of advection.

One can, in general, notice that the errors seem to be more dependent on k than on the actual advection time $n\Delta t$. The errors are symmetric around $k = \pm 0.5$, since the advection of $|\delta x|$ in the positive direction is equivalent to advection of $|\Delta x - \delta x|$ in the negative direction from the next gridpoint. Also, there are maxima in error at $k = \pm 0.5$, since it is the maximum one can advect in one direction without it becoming equivalent to negative advection from the next gridpoint in the opposite direction.

A.1.2 Initial Gaussian Profile

We initialize with the profile:

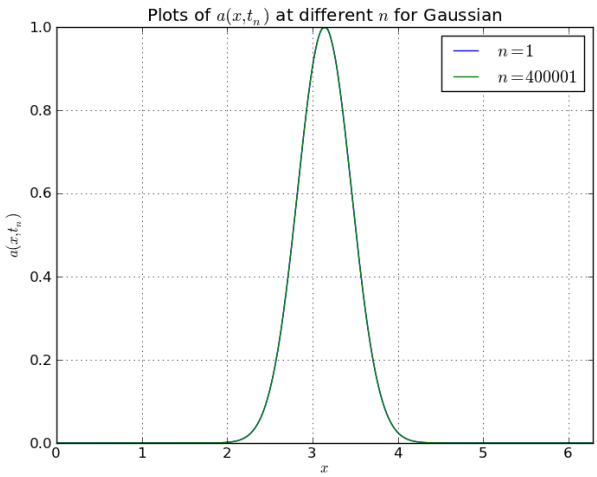

(a) Plot of Waveform, $k = 0.99$

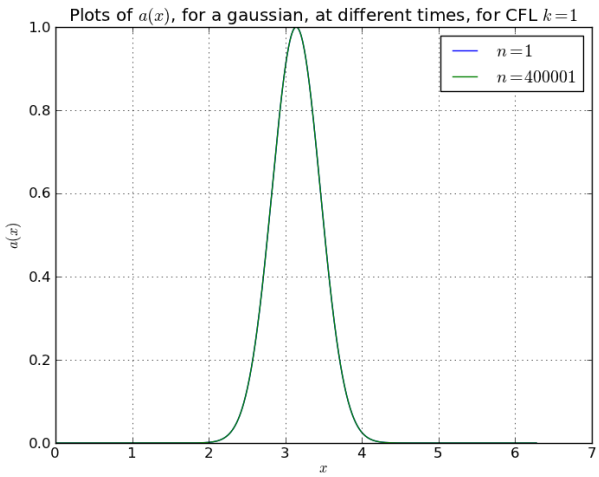

(b) Plot of Waveform, $k = 1$

Figure A.5: Plots of the Waveform at the beginning and the end of the advection for $k = 0.99$ and $k = 1$, for initialized Gaussian.

$$a(x,0) = \exp\left(-\frac{1}{2}\frac{(x-\pi)^2}{0.1}\right),\ 0 \leq x < 2\pi \tag{A.4}$$

As we have already performed a comparison for the error in a periodic initial condition, we now choose an initial condition that somewhat pertains to waveforms that we may have to deal with, in physical situations. It is for this purpose, that this (unnormalized) Gaussian was chosen. The plots for the initial and final advected waveforms, both values of k, can be found in figure (A.5).

One can see that these plots are, similar to the previous case, not noticeably different. Thus, we can see that the algorithm has no difficulty handling an analytically non-periodic waveform, upon which periodic boundary conditions have been imposed.

A.1.3 Initial Square Wave Profile

The initial waveform is:

$$a(x,0) = \begin{cases} 1 & \pi/2 \leq x \leq 3\pi/4 \\ 0 & \text{otherwise} \end{cases} \tag{A.5}$$

We have initialized this to check the efficacy of the discontinuity detection algorithm. This is because pure advection preserves the waveform in its exact shape. However, numerical methods inadvertently introduce a dissipation. We wish to see how the discontinuity detection algorithm accounts for the dissipation. To characterize this, the values of the tolerances are kept the same as that of Colella-Woodward[24]:

$$\eta^{(1)} = 20,\ \eta^{(2)} = 0.05,\ \epsilon = 0.01 \tag{A.6}$$

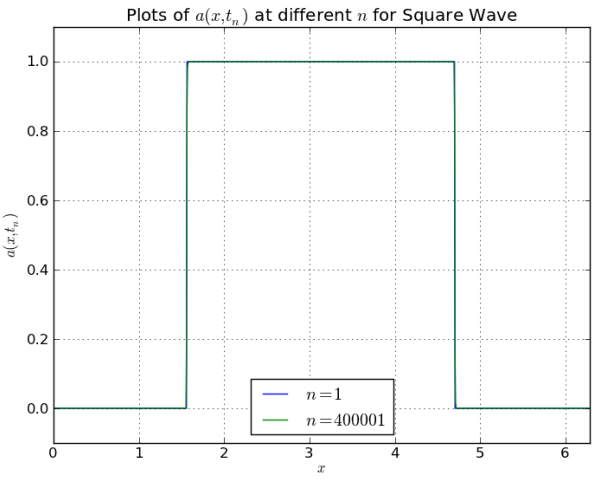

(a) Plot of Waveform, $k = 0.99$

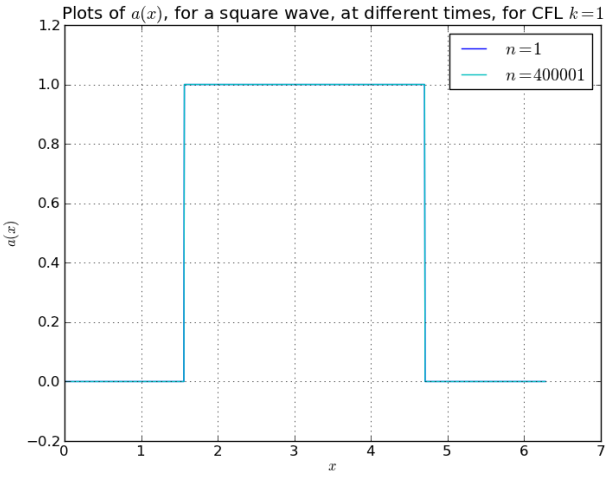

(b) Plot of Waveform, $k = 1$

Figure A.6: Plots of the Waveform at the beginning and the end of the advection for $k = 0.99$ and $k = 1$, for an initial Square Wave.

The plots of the initial and advected waveform are in figure (A.6). In case of $k = 1$, there is virtually no change in the wavefunction, and the advection is near perfect. In case of $k = 0.99$, however, there is a minor decay at the discontinuities and that error (as compared to the initial waveform), is plotted in figure (A.7).

A.2 Fourier Transform based Solution for the Poisson Equation

We perform the following benchmarks:

1. A periodic sine function with both the mentioned methods, to check the accuracy of both the methods.

2. A sharply peaked Gaussian with a flat tail, in order to demonstrate the accuracy when the function displays periodic boundary conditions, despite the analytical function used to generate the function not being periodic.

The size of the grid and rest of the tunable parameters are same as that in the previous subsection.

A.2.1 Initial Sine Profile

The initial profile chosen is:

$$\rho(x) = \cos x, \ 0 \leq x < 2\pi \tag{A.7}$$

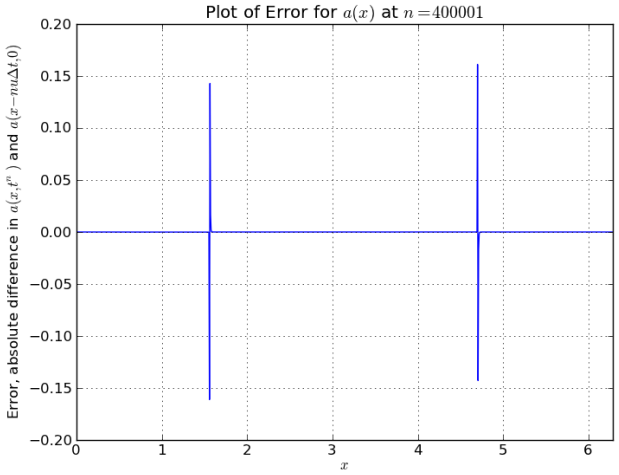

Figure A.7: Plot (for k=0.99) of the error for initial square wave, at the end of the advection $n = 400000$.

and the error is calculated by the expression:

$$\delta E(x) = |E(x) - \sin x| \tag{A.8}$$

The plot for the solutions, by both Methods I(2.15) and II(2.16), are plotted in figure (A.8). Therefore, we plot the errors for both the methods (figure (A.9)). One can see that the error in Method I is much lesser than that of Method II. This is to be expected as the former is derived analytically, and the latter is derived by discrete Fourier transform on divided differences, prone to error.

A.2.2 Initial Gaussian Profile

We initialize the profile:

$$\rho(x) = \exp\left(-\frac{1}{2}\frac{(x-\pi)^2}{0.1}\right),\ 0 \leq x < 2\pi \tag{A.9}$$

The plots of the solutions by both the methods and the analytical solution can be found in figure (A.10). One can see that one cannot discern any difference in the three plots. Therefore, we plot the error (figure (A.11)). One can see a similar result as to the previous case. Also, we have shown that the algorithm can handle analytically non periodic functions as long as periodic boundary conditions are imposed under some limits (in this case we chose to apply them at $x = 0, 2\pi$ as the tail was sufficiently flat enough). It would also be interesting to study the dependence of the error in $E(x)$ on position x, which we see from the figures A.9 and A.11.

Now, since both the components have been benchmarked, we proceed to assemble the solver for the Vlasov-Poisson system.

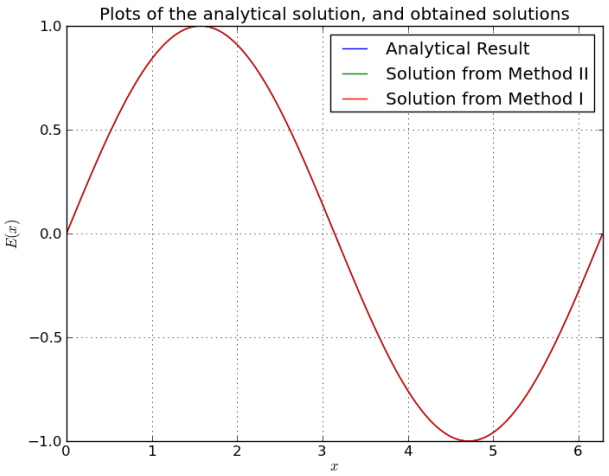

Figure A.8: Plots of the analytic and obtained solutions for the Poisson equation. One can not discern any difference between the analytical and the computational solution.

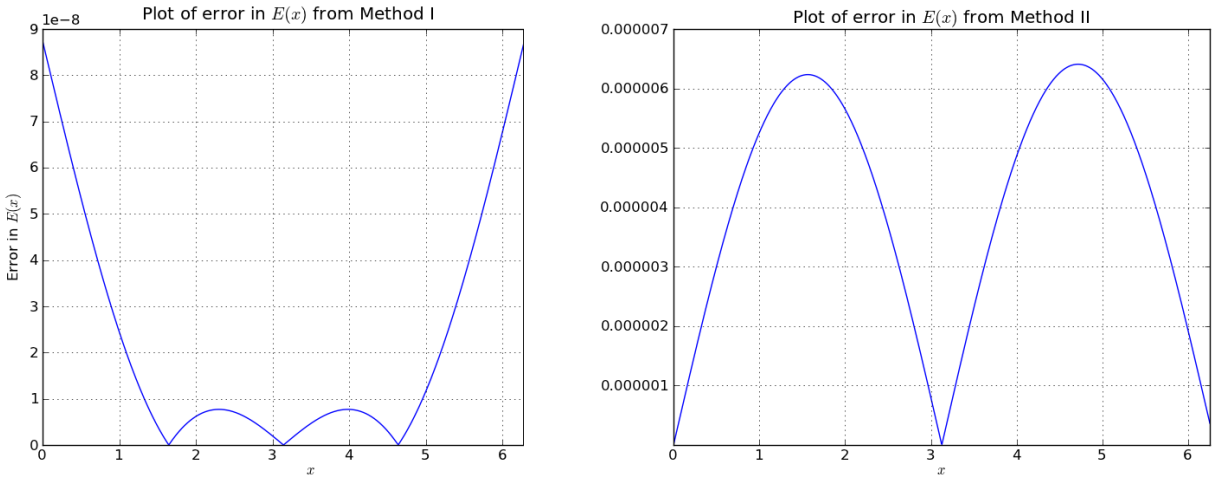

(a) Error for Method I

(b) Error for Method II

Figure A.9: Plots of error in the electric field, $\delta E(x)$, for Methods I and II, for a cosine charge density profile.

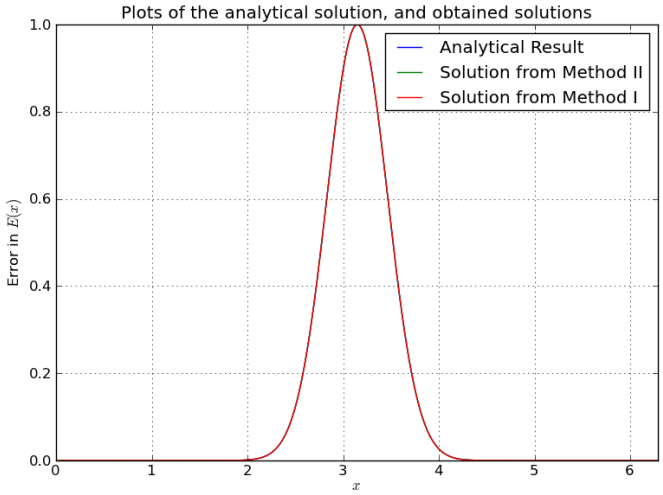

Figure A.10: Plots of the analytic and obtained solutions for the Gaussian equation. Again, one can not discern any difference between the analytical and the computational solution.

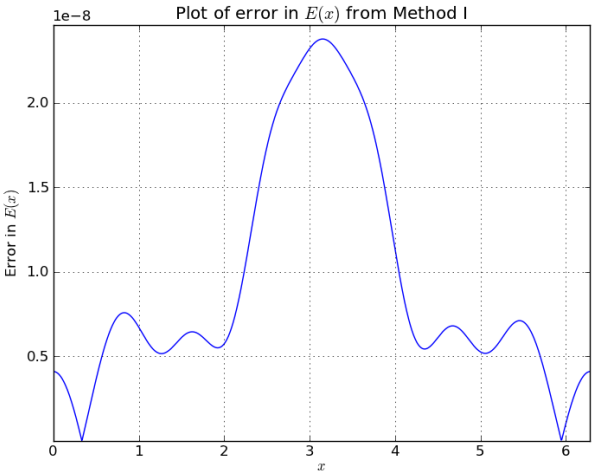

(a) Error for Method I

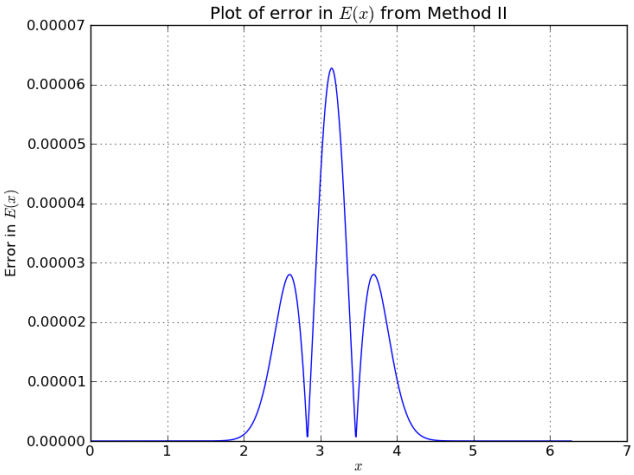

(b) Error for Method II

Figure A.11: Plots of error in the electric field, $\delta E(x)$, for Methods I and II, for the derivative of the Gaussian set as the initial charge density.

Appendix B

Benchmarking the Vlasov-Poisson Solver

In this appendix, we benchmark the Vlasov-Poisson solver it to study its features and limitations. We fix a few conditions for the sake of the uniformity of results. We have applied periodic boundary conditions on both spatial and velocity domains. Periodic boundary condition(PBC) on velocity domain may not be physical, however, accounting for the size of the distribution function, and setting the velocity domain limits in such a way that the velocity distribution function has a flat tail as it approaches the boundaries, mitigates any unphysical effect on the distribution function caused by the PBCs [26]. The spatial domain is defined as $0 < x < L$ and the velocity domain is defined as $-v^e_{max} < v < v^e_{max}$, where e superscript denotes the electron velocity. L is usually defined as $L = 2\pi/k$ (unless specified), where k is the value of the perturbed mode. v^e_{max} varies as per the benchmark test, because it is defined depending on the velocity distribution function used. Also, for the purpose of the benchmark, which relies on previously obtained results, we disable the discontinuity detection algorithm from the PPM module of the program. Unless otherwise mentioned, we use the regular timestep algorithm.

B.1 Linear Landau Damping

For collisonless plasmas, where damping by collisions is negligible, a damping (or acceleration) phenomenon called linear landau damping is observed. Theoretically, this phenomenon is observed by choosing a correct contour for the integration of the dispersion relation[2]. This is necessary, because one must account for a singularity that otherwise lies off the path of integration. This was first correctly done by Landau[1]. Physically, the particles of the plasma that travel at nearly the phase velocity of the plasma wave do not see a time-dependent value of the electric field and hence can exchange energy with the wave. Thus, damping happens because a fraction of the particles that are going slightly faster than the phase velocity of the plasma wave slow down by giving energy to the wave. Similarly those that are slightly slower than the wave gain energy from the wave and accelerate (in which case the phenomenon is called Landau acceleration)[2].

We set a system with a small perturbation over the equilibrium Maxwellian. Now, we aim to study this by numerical solution of the system. This serves as a useful benchmark because such a system is also analytical solvable under the linear limit. Thus, one can compare the numerical results with the analytical ones. Following Vann-Arber[22], we set the initial distribution function to be:

$$f(x, v, 0) = (1 + \alpha \cos(kx)) \exp(-v^2/2)/\sqrt{2\pi} \tag{B.1}$$

where α and k are the tunable parameters. The parameters chosen are:

$$v^e_{max} = 4.5,\ \alpha = 0.01,\ k = 0.5 \tag{B.2}$$

We vary the gridsize, in x, between $N_x = 32$ and $N_x = 512$, and in v, between $N_v = 32$ to $N_v = 512$, both in multiples of 2. This is done so as to establish a pattern in the errors of the linear landau damping rate γ, and the energy E and momentum p, with gridsize.

B.1.1 Benchmark for the damping rate γ

The rate of linear landau damping γ is calculated by the following procedure:

1. We calculate the amplitude of the fundamental harmonic of the electric field $|E_1|$, by Fourier transform of the electric field $E(x, t)$ (the obtained values have to be normalized by $N_x/\sqrt{2\pi}$. We have not done so for these tests as we want to compare the slopes of the logarithm of $|E_1|$ only. A multiplicative constant only displaces the curve in the $y-$axis, and does not affect the slope of the curve. Also from here on, any reference to the harmonics of the electric field refer to the modulus of its value, unless specified.)

2. We plot the natural logarithm of $|E_1|$ with time.

3. We fit a straight line through the the maxima of the plot, using the linear least squares fit. Now, we know that linear landau damping is only valid till the bounce time $\tau_b = 2\pi(\alpha)^{-1/2}$ of trapped electrons[21, 22]. α in (B.2), is the strength of perturbation. Here, for $\alpha = 0.01$, $\tau_b \sim 62.8$. Also, for a small perturbation, such as our initial condition, the damping phenomenon will show recurrence at time $T_R = 2\pi/k\Delta v$. T_R is referred to as the "Recurrence time." Thus, we choose maxima till time $T_R/2$ (for $N_v = 32$) and till $t \sim 44.7$ (which is $T_R/2$ for $N_v = 64$, and would provide a common yardstick to test the accuracy for $N_v \geq 64$. Also, it should be noted that for $N_x = 32$, $\tau_b > T_R$ and, for $N_x = 64$, $\tau_b > T_R/2$.)

4. The slope of the fit straight line is the value of γ. The theoretical calculated value of γ is -0.153359[22], for the parameters used, against which we compare its accuracy. Also, one should note that the theoretical value of γ is only valid for late time[22], so the errors calculated are merely deviations.

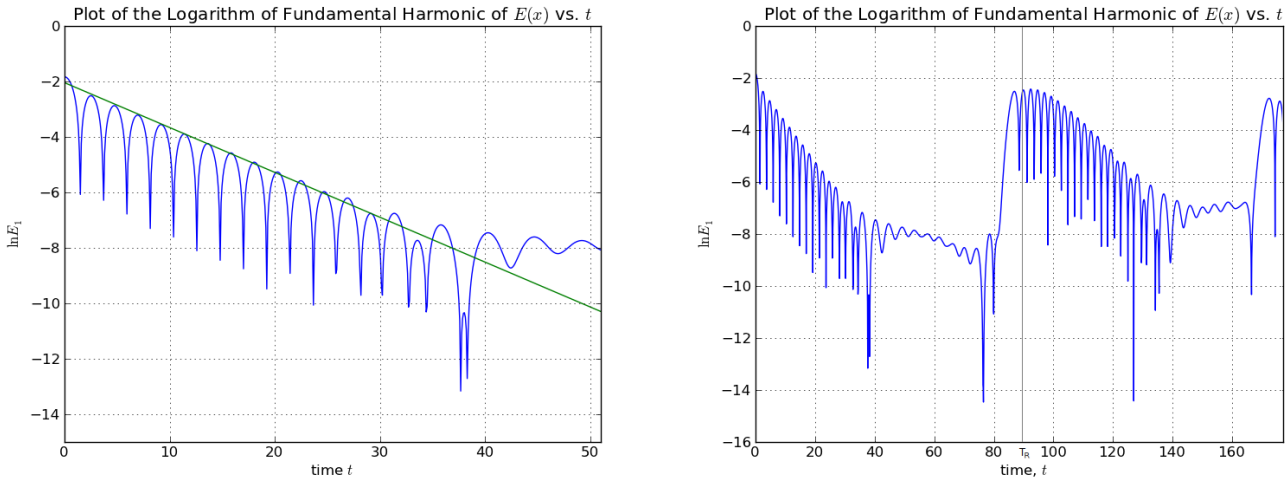

(a) Fit of a straight line through the maxima of $\log|E_1|$.

(b) Example of Recurrence. Here recurrence is at $T_R \sim 89.36$.

Figure B.1: Examples of straight line fit and recurrence on a 32×64 grid, for linear landau damping. A vertical line has been drawn at $t = T_R$ in (b) to show the recurrence time. One can also notice that the system is about to recur again at about the end of the simulation.

$\downarrow N_v, N_x \rightarrow$	32	64	128	256	512	$\gamma, N_x = 512$
32	3.39	3.39	3.34	3.48	3.41	-0.15858331
64	5.49	6.56	6.79	6.88	6.88	-0.16391231
128	0.65	0.83	0.86	0.86	0.86	-0.15467647
256	0.03	0.22	0.24	0.25	0.25	-0.15373746
512	0.06	0.18	0.25	0.25	0.25	-0.15373604
$\gamma, N_v = 512$	-0.15344989	-0.15363378	-0.15374081	-0.15374608	-0.15373604	γ

Table B.1: Table of absolute percentage error in γ against theoretical $\gamma = -0.153359$. The values of γ obtained for the gridsizes $N_x = 512$, and $N_v = 512$ have been shown as a reference.

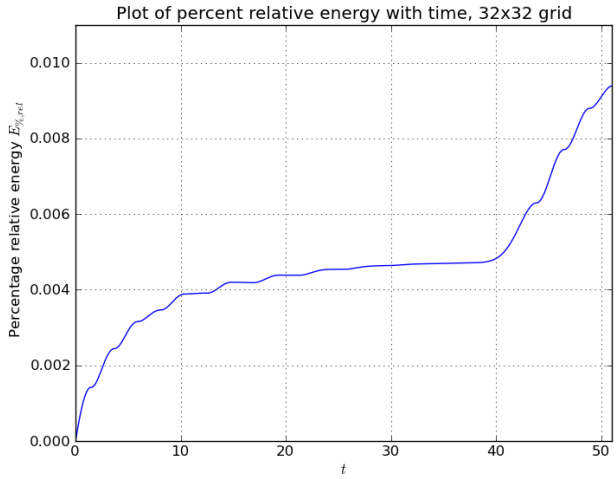

(a) Plot of percentage energy relative to initial value.

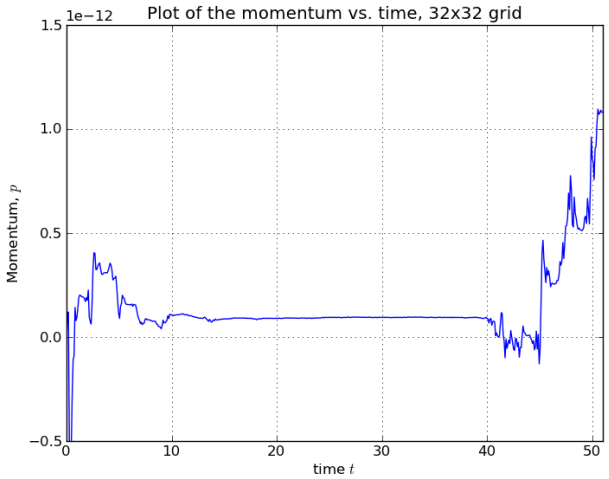

(b) Plot of momentum p.

Figure B.2: Plots for percent relative energy and momentum, for a 32×32 grid.

As an example of the fit and recurrence, one can refer to figure (B.1). This looks similar to Fig. 1 of Vann-Arber[22]. The absolute percentage errors for for the gridsizes are in table (B.1). One can see that increasing the dimensions has a limited effect on the accuracy. However, since these errors are deviations, we can say that as the gridsize increases there is some convergence of the error value to ~ 0.25. This means that beyond a certain gridsize, accuracy doesn't increase appreciably. Also, the percentage errors for $N_v = 32$ and $N_v = 64$ have a marked difference because of the number of points used for the fit (as decided earlier). Furthermore, one can see that increasing $N_v > 64$ decreases the error. However, increasing N_x doesn't seem to have any significant effect on the error. This demonstrates that Landau damping is indeed a velocity-space dependent, or in other words, a kinetic phenomenon.

B.1.2 Test for conservation properties of the solver.

Now, we compare the energy and momentum conservation properties for various gridsizes. For a 32×32 grid, we can see the energy and momentum plots in figure (B.2). Percent relative energy is defined as:

$$E_{\%,rel} = \frac{E_{total}(t) - E_{total}(0)}{E_{total}(0)} \times 100\% \tag{B.3}$$

where E_{total} is computed as:

$$E_{total}(t) = T(t) + V(t),\ T(t) = \int\int dxdv\ v^2 f(x,v,t),\ V(t) = \int dx\ (E(x,t))^2 \tag{B.4}$$

The actual total energy, at any given, is the half of $E_{total}(t)$. However, $E_{\%,rel}$ remains same irrespective of the factor of half.

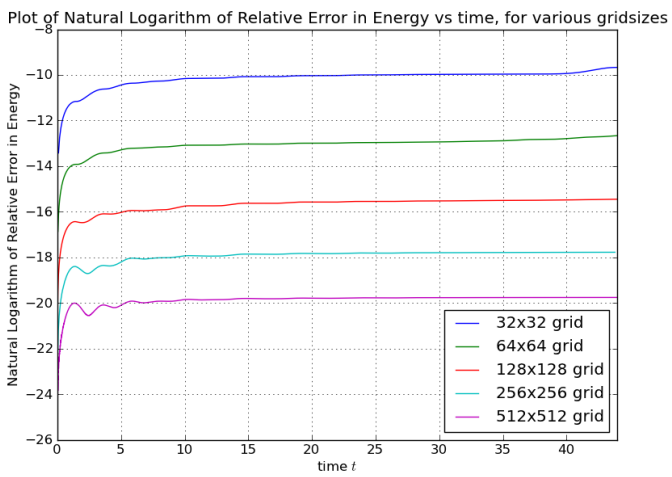

(a) Plot of percentage energy relative to initial value.

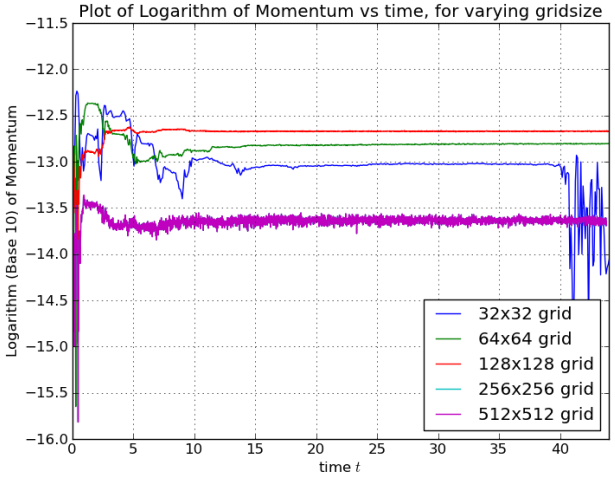

(b) Plot of momentum.

Figure B.3: Plots for percent relative energy and momentum, for varying gridsize.

One can see that energy remains conserved to 0.01% of the the initial value, and momentum fluctuates in the order of 10^{-12}, which is very close to zero as expected. It would be interesting to see how these values scale with the gridsize. So, we plot the logarithm of the corresponding values of the relative energy and absolute value of momentum. (Natural logarithm has been taken on relative energy and base 10 logarithm has been taken on momentum. This is because, in case of momentum, we wish to see how close to machine precision, lie the values of momenta.) This is shown in figure (B.3). We can see that, with increasing gridsize, both the energy and momentum conservation improve.

We would also like to see how these qualities scale with individual sizes of dimensions. So, we fix one dimension to 512 and vary the other. Plots for those can be seen in figure(B.4). It is noticeable that on increasing N_x and N_v by 2, energy conservation increases by order of $\sim e$ and $\sim 2e$ respectively. With momentum conservation, increasing N_x (from 32 to 512) improves conservation by a difference of about one and a half orders, however, increasing N_v (from 32 to 512) is not that effective and settles to an improvement of one order.

As we saw with the PPM advection solver, an error of $O(\Delta x)$ develops at the peaks of the function being advected. Therefore, it is worthwhile to check whether increasing the strength of perturbation (i.e. α) has any effect on the conservation of energy and momentum. This is because, a higher value of α creates more peaks in the distribution along x, and these peaks may gather errors during advection that affect the corresponding energy and momentum. Therefore, to get an idea of this, we choose the amplitudes of strength of perturbation $\alpha = \{0.01, 0.02, 0.03, 0.05, 0.1, 0.2\}$ to check for these errors. Also, we fix a gridsize of 64×64 for this particular test. The plot of the logarithms of the relative energy and absolute value of momentum can be seen in figure (B.5).

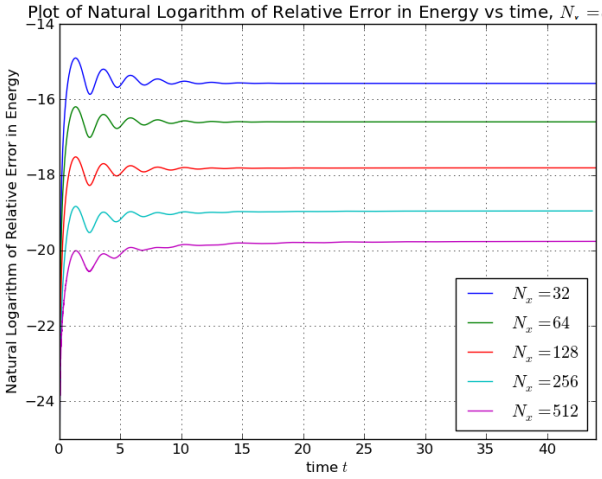

(a) Plot of percentage energy relative to initial value. Varying N_x.

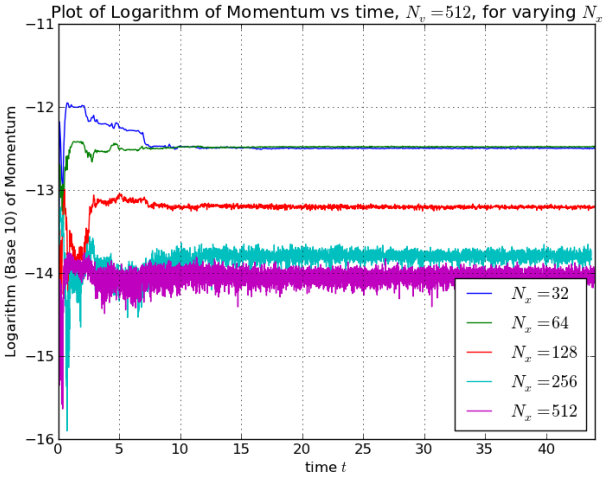

(b) Plot of momentum. Varying N_x

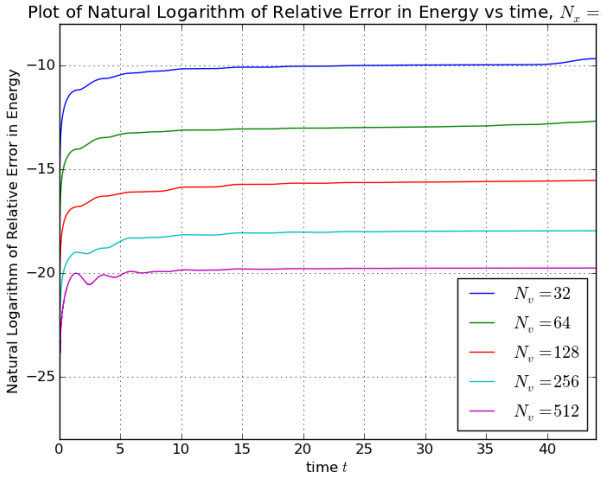

(c) Plot of percentage energy relative to initial value. Varying N_v.

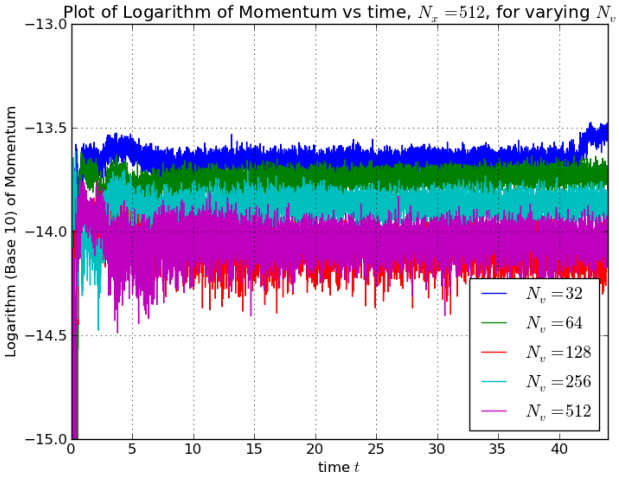

(d) Plot of momentum. Varying N_v

Figure B.4: Plots for percent relative energy and momentum, for varying individual dimension size.

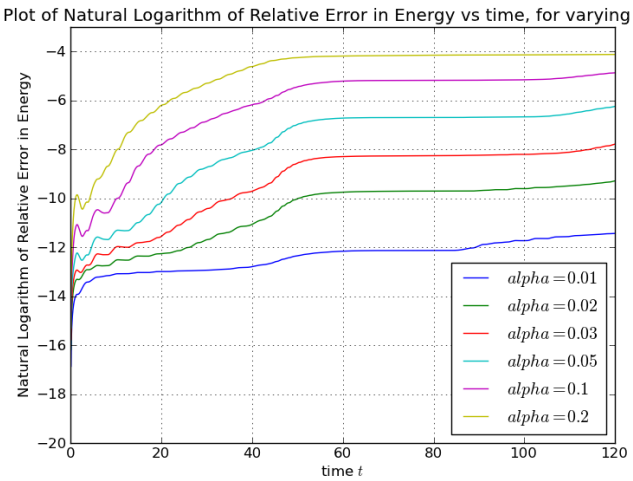

(a) Plot of percentage energy relative to initial value.

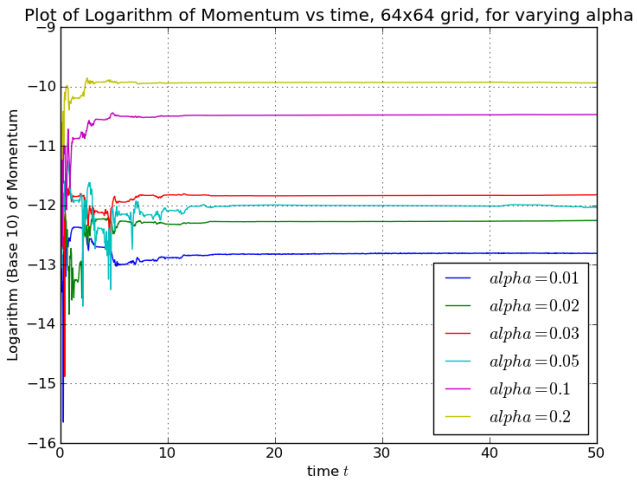

(b) Plot of momentum.

Figure B.5: Plots for percent relative energy and momentum, for different α.

As we can see, on increasing α from 0.01 to 0.2, relative energy conservation deteriorates by about 8 orders of e, and momentum conservation decreases by 3 orders of 10. As mentioned, this may be because of errors accumulated by the peaks during advection.

B.1.3 Benchmarking the large timestep algorithm

Now, we wish to check for the accuracy of the large timestep algorithm, which we use in the PPM advection solver to circumvent the CFL condition. We apply this solver and plot the results. Creating plots for errors is difficult because an analytic solution is not available to compare the results for different timestep sizes. Also, comparing one with the another is not useful, as with different stepsize, the number of data points in time changes. Now, the plots for evolution of fundamental harmonic of electric field $\ln |E_1|$ with time, for various timestep sizes and gridsizes can be found in figure (B.6).

The CFL number k in the plots refers to the maximum value of k encountered by the solver in advancement of one timestep. It is calculated by:

$$k = v^e_{max} \frac{\Delta t}{\Delta x} \tag{B.5}$$

With the large timestep algorithm enabled, we have plotted the $k < 1$ graph as a reference solution, as we increase timestep size. As one can see one can notice virtually no difference in the plots for different gridsizes (except $\Delta t = 0.4$, which clearly offshoots visibly, irrespective of gridsize.) One can study the displacement from the reference solution by zooming into the graph at later timesteps, when landau damping would damp the value of the electric field, and the errors appear exaggerated. Two such figures for 64×64 and 512×512 gridsize have been shown in figure (B.7). Also, we fit the maxima of the plot

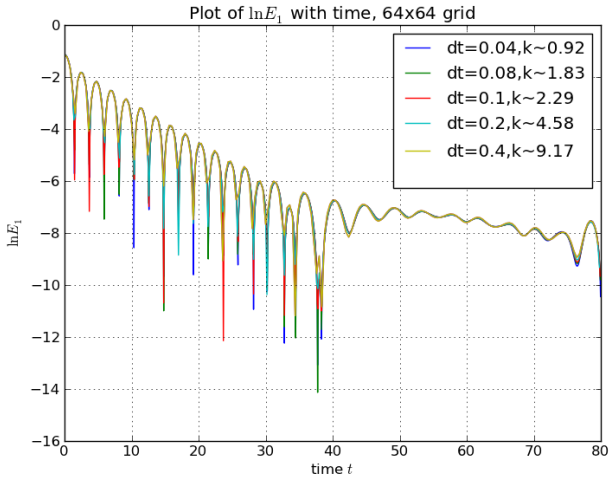

(a) 64×64 grid.

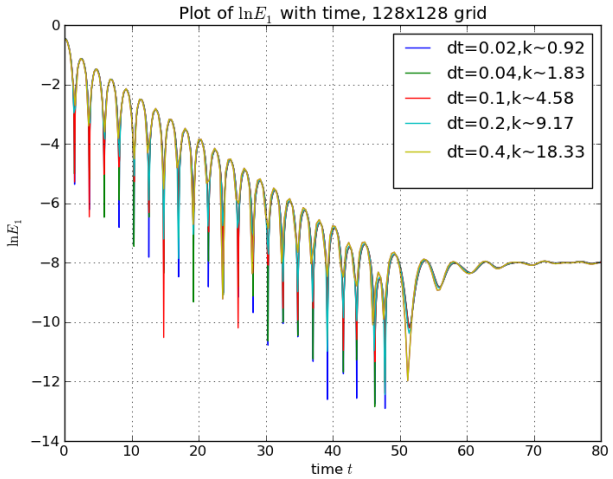

(b) 128×128 grid.

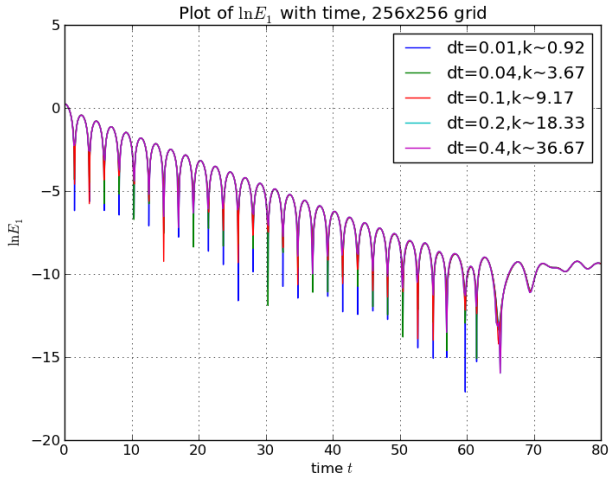

(c) 256×256 grid.

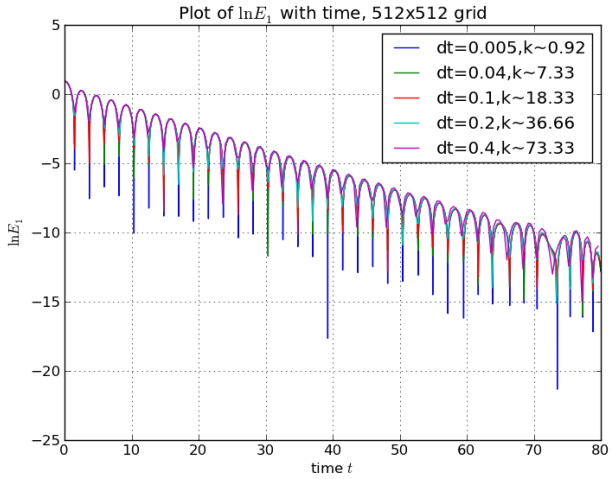

(d) 512×512 grid.

Figure B.6: Plots for (unnormalized) fundamental harmonic of electric field $\ln |E_1|$, for various timestep sizes, on various gridsizes. Legend contains the timestep size and the value of the CFL number k, for corresponding gridsize.

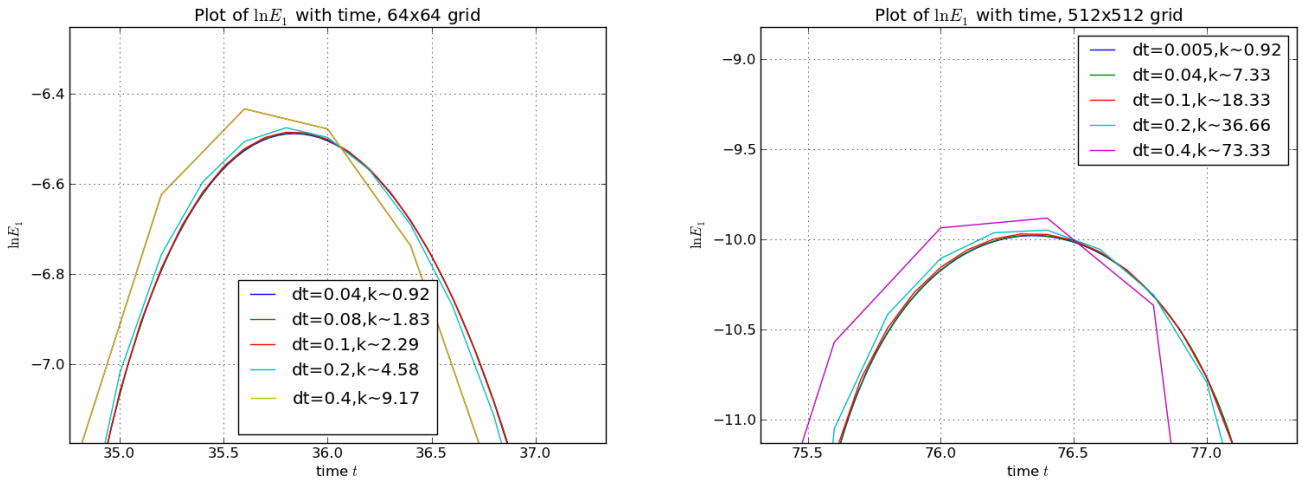

(a) 64×64 grid.

(b) 512×512 grid.

Figure B.7: Plots (zoomed after most of the damping is over) for (unnormalized) fundamental harmonic of electric field $\ln |E_1|$, for various timestep sizes, on various gridsizes. Legend contains the timestep size and the value of the CFL number k, for corresponding gridsize. Since this zoom is performed after most of the damping is over, it reflects the errors in $\ln |E_1|$ for small orders of $|E_1|$. Thus, any error in $|E_1|$ should have cumulatively accumulated till this time. This would help us discern the errors corresponding to the values of k.

to a straight line to find the rate of damping γ. We tablulate the percentage errors in γ against the value of the CFL number k to search for an empirical relation between k and errors.

As one can see, the order of the values are roughly the same, but the $\Delta t = 0.4$ plot has offshot clearly. Also $\Delta t = 0.2$ is slightly, though much lesser than the previous one, displaced. However, $\Delta t = 0.1$ follows the reference solution closely, and is not discernible from it even in this zoomed picture.

Now from table B.2, one can see that the errors in γ, seem to become lesser as the gridsize increases. This is similar to the result we obtained before. Also, the errors become lesser as the value of k increases. However, for the highest k in each column (which corresponds to $\Delta t = 0.4$), most of the errors have again offshot in the other direction. The errors are the least for $\Delta t = 0.2$ (which correspond to the second highest value of k in each column), however one has to remember that the solution has already offshot from the reference solution.

Now we notice that, even though these gridsizes are disparate, the behaviour of the solution with time doesn't seem to depend much on the gridsize, and instead, seems to solely depend on the value of Δt. This is consistent with the choice of timestep size by Ghizzo, et al[26]. They have arrived at a result for the choice timestep size, which is

$\downarrow k$, gridsize $\rightarrow$	64×64	128×128	128×128	512×512
0.92	6.56	0.86	0.25	0.25
1.83	6.33	0.83	-	-
2.29	6.25	-	-	-
3.67	-	-	0.23	-
4.58	5.02	0.78	-	-
7.33	-	-	-	0.20
9.17	1.57	0.70	0.18	-
18.33	-	-0.94	0.14	0.18
36.66	-	-	-1.44	-0.01
73.33	-	-	-	-1.43

Table B.2: Table for the percentage errors in values of γ. These are obtained by the same fitting method used at the beginning of the subsection. Tabulated against values of CFL number k and the gridsize. The entries '-' mean that no run has been given for that value of 'k.' Depending on the gridsize, we have only given a run for those values of k which show a significant deviation from the reference solution. Also, for smaller gridsizes, larger values of k have been omitted because we have already shown that the errors have offshot for a particular value of k.

independent of gridsize (using Shannon theorem):

$$\omega_p \Delta t \ll 1 \tag{B.6}$$

and since we have normalized time by plasma frequency ω_p anyhow, this simplifies to $\Delta t \ll 1$. Ghizzo, et al. have chosen $\Delta t = 0.25$. We have shown that $\Delta t = 0.4$ is accurate in order but does not resemble the reference solution closely and its errors also offshoot. $\Delta t = 0.2$, in our solver, generates more accurate values of γ, but is visibly displaced from the reference solution.

Thus, looking at Fig. B.7 and Table B.2, we can empirically say that, a value of Δt that corresponds to a CFL number k, such that $k \leq (0.05 \times N_x)$, will result in a solution which closely follows the reference solution. (We have said N_x in the previous formula because, usually we choose $N_v \geq N_x$).

Also, it would be interesting to see how energy scales with time. This can be seen in figure (B.8). One can see from the plot how errors increase with timestep size. This is where the error of $O((\Delta t)^3)$ from Strang splitting becomes apparent. Till here, we have summarized the results we have obtained from the study of linear landau damping. We have purposely not studied entropy because of the small perturbation, which doesn't lead to any appreciable change in entropy over time. This results entropy being a weak diagnostic for linear landau damping. It becomes useful in the next section, where the perturbation is visibly larger. Also, we have to mention that entropy doesn't become undefined anywhere in these simulations. This is an indication that the positivity of the distribution function is being maintained at all times. This is because, in the entropy diagnostic, we have deliberately not included a check in case of negative distribution function, and thus would acquire an unrepresentable value (NaN), if $f(x, v, t)$ ever became

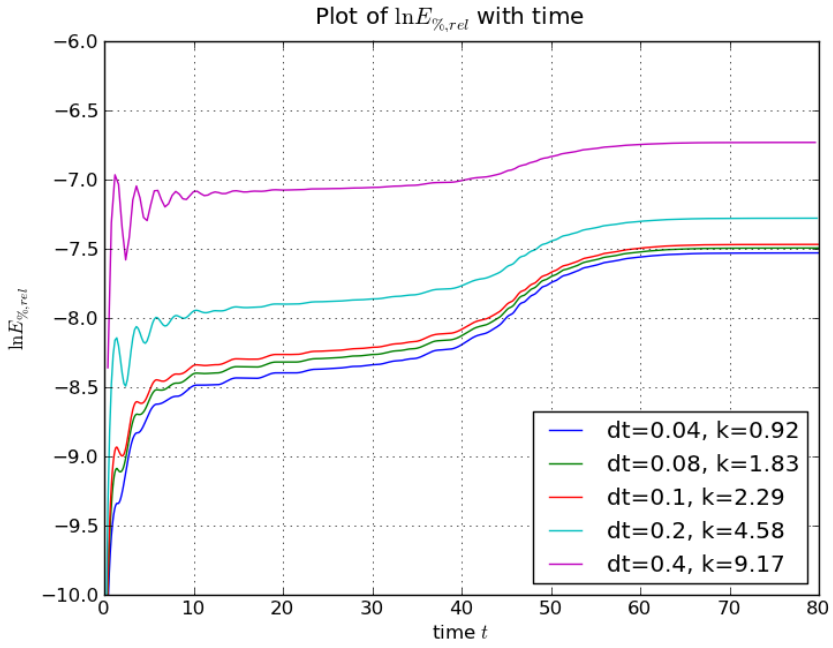

Figure B.8: Plots of natural logarithm of percent relative energy, $\ln E_{\%,rel}$, with time, on a 64×64 gridsize.

negative. This doesn't happen with any of the above simulations. This is an indication of how well the PPM advection method maintains the positivity of $f(x, v, t)$, primarily because of the monotonicity limiters.

Also, just to check how the Vlasov-Poisson solver behaves if it ever encountered a negative distribution function, we initialize an unphysical distribution function as follows:

$$f(x, v, 0) = (1 + \alpha \cos(kx)) \frac{\exp(-v^2/2) \cos\left(\frac{\pi v}{v^e_{max}}\right)}{\int dv \ \exp(-v^2/2) \cos\left(\frac{\pi v}{v^e_{max}}\right)} \tag{B.7}$$

where the denominator in the RHS is just for normalization. All other constants are kept the same ($\alpha = 0.01, v^e_{max} = 4.5, k = 0.5$)as in the beginning of the subsection. Also, we use the regular timestep algorithm to determine the timestep. This function is smoothly negative in regions of $|v| > 2.25$. We run this initial condition on a gridsize of 64×64 up to about $t = 180$. We show the time evolution of the fundamental harmonic of the electric field $\ln |E_1|$, just to see how the process of linear landau damping adapts to this unphysicality (figure B.9). As one can see, the rate of landau damping is much lesser than in the normal case, and is practically undamped till recurrence time $T_R = 89$. Thus the perturbations have an effect other than damping. In order to see this, we define (unnormalized) velocity distribution function $f(v)$:

$$f(v, t) = \int dx \ f(x, v, t) \tag{B.8}$$

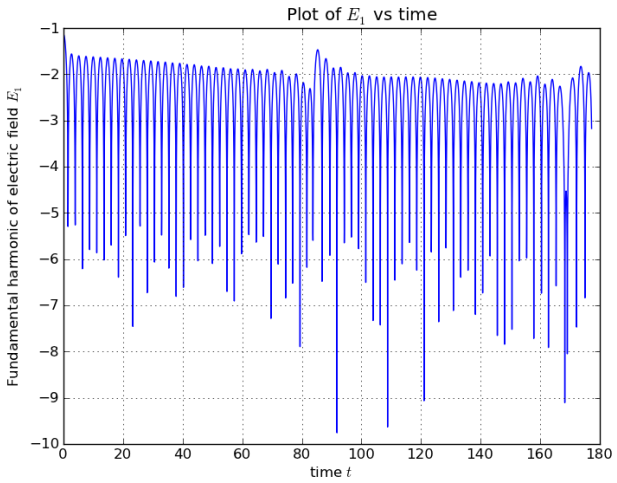

Figure B.9: Plot of the logarithm of the fundamental harmonic of the electric field $\ln |E_1|$ with time, for initial distribution function (B.7), on a 64×64 grid.

From here on, $f(v,t)$ which is written without x as an independent variable will denote the unnormalized velocity distribution function. We plot $f(v)$ at different times during the simulation to see its behavior (Fig. B.10).

It can be seen that the extrema $f(v)$ decay slightly, with time, at the extrema, but is otherwise unchanged. In other words, the distribution function, if initialized as negative in some region remain negative in those regions. As a corollary, we can say that the solver would maintain an initially positive distribution function to remain positive, by similar mechanisms.

Now, we also notice that the positive extremum decays a little with time. Therefore, we zoom the area around one negative extremum. This can be seen in figure (B.11). One can see that, with time, this extremum also decays toward zero, again by a small amount. Therefore, the effect of the perturbation is to decay the extrema by small values. This improvement may not speak much for this case, however it is really crucial for the case of physical initial conditions. Now suppose that, at some timestep, the distribution function became negative. Now, on the judicial choice of timestep, as we have discussed earlier, at any given time, the distribution function won't become too negative too quickly. Thus, the distribution function can be assumed to have developed a region of small negativity. Meanwhile, the solver would have pushed back this small negative region to become positive. Thus, in the event the the distribution function were to become negative, the solver would simultaneously push it to become non-negative.

Thus, we now know that the solver tries to maintain the sign of the distribution function values similar to the initial condition and that regions that would have developed small negative values would be pushed back to become non-negative. Now we move on to discuss the behaviour of the Vlasov-Poisson solver in case of a larger perturbation.

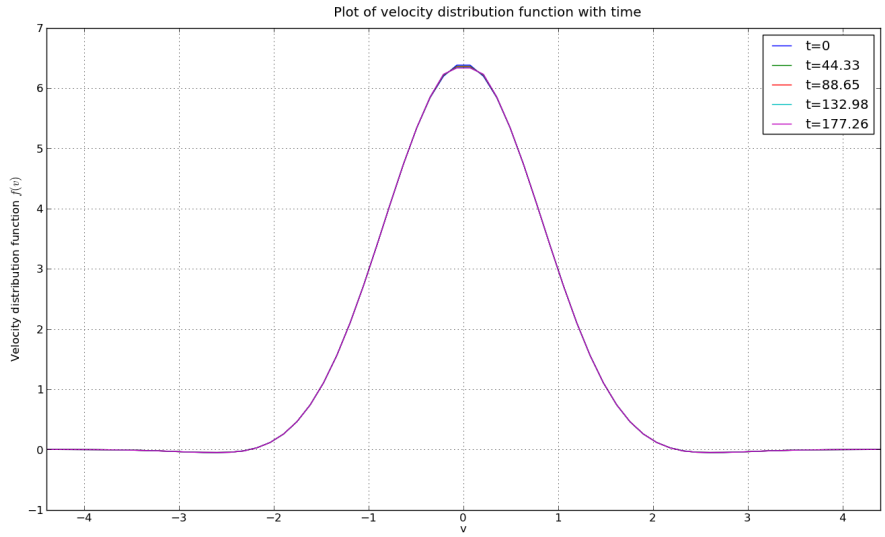

Figure B.10: Plot of the (unnormalized) velocity distribution function at different times, for initial distribution function (B.7), on a 64×64 grid.

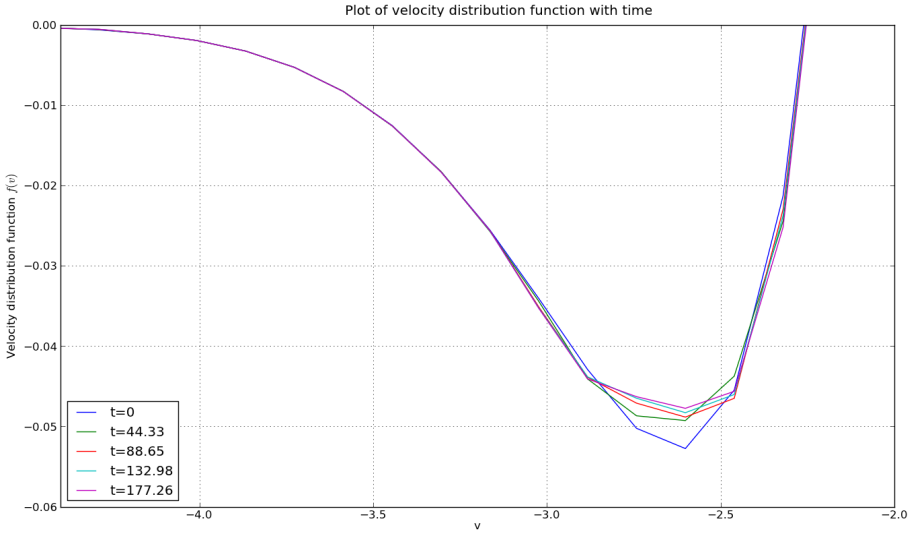

Figure B.11: Zoom of the negative region of the (unnormalized) velocity distribution function at different times, for initial distribution function (B.7), on a 64×64 grid.

B.2 Bump-On-Tail Instability

The bump-on-tail distribution corresponds to:

$$f(x,v,0) = (1 + \alpha\cos(kx))f_{bot}(v,0) \tag{B.9}$$

where the Bump-on-Tail(B.o.T.) velocity distribution function is given by:

$$f_{bot}(v,0) = n_p \exp\left(-\frac{1}{2}v^2\right) + n_b \exp\left(-\frac{1}{2}\frac{(v-v_b)^2}{v_t^2}\right) \tag{B.10}$$

where the normalization constants are, for the plasma, $n_p = 0.9/\sqrt{2\pi}$ and, for the beam, $n_b = 0.2/\sqrt{2\pi}$. For this case, we choose the tunable parameters as:

$$\alpha = 0.04,\ k = 0.3,\ v_b = 4.5,\ v_t = 0.5,\ v^e_{max} = 6 \tag{B.11}$$

Physically, this initial velocity distribution $f_{bot}(v,0)$ represents the introduction of a Maxwellian beam of energetic electrons into a Maxwellian plasma (assuming a constant neutralizing ion background). The beam has an average velocity of $v_b = 4.5$. We perturb this system, further, with $\alpha\cos(kx)$ perturbation. Thus this simulation essentially represents the interaction of a beam with plasma, for a small perturbation. It is called a "beam-plasma instability" because of a small value for n_b. For larger values of n_b, the physical situation would correspond to a "two-stream instability."[2]

Now, the monotonicity algorithm of the PPM advection solver, primarily introduces a dissipation, and, hence, the solver damps any fine-scale structures that would have otherwise grown with time. Thus, as these numerical artifacts are corrected for, the system is more quickly drawn to a stable BGK mode[22]. To see this, we study the evolution of maximum of the absolute value of electric field $|E|_{max}$ with time. This is plotted in figure (B.12), on a 128×128 grid.

For a more refined image, we repeat it on a 512×512, and the choice of axes is made so that it can be compared with Fig. 3 of Arber and Vann[22]. This is seen in figure (B.13).

Now, we can say that this is settling to a stable state, if the entropy doesn't vary much at later times. So, we plot the graphs for relative entropy, defined as:

$$S_{rel}(t) = \frac{S(t) - S(0)}{S(0)} \tag{B.12}$$

where we have:

$$S(t) = -\int\int dxdv\ f(x,v,t)\ln f(x,v,t) \tag{B.13}$$

This can be seen in figure (B.14). One can see that S_{rel} tends to stabilize quicker, and at a lower value, in the 512×512 gridsize simulation than in 128×128. Now, we would like to see how the phase-space looks like, so we plot at $t \sim 512$, the distribution function, where the perturbation is present. This can be seen in figure (B.15).

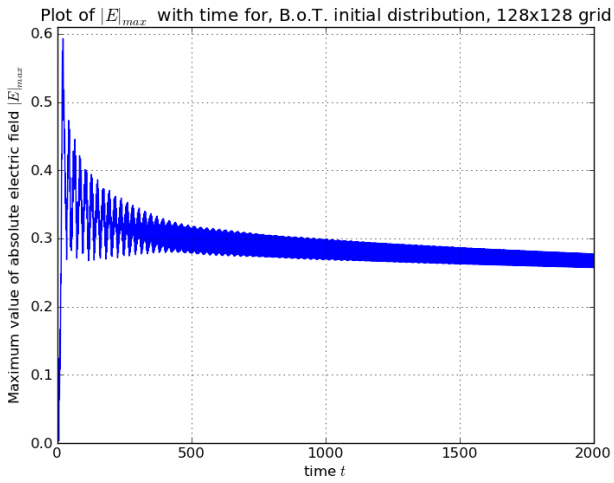

Figure B.12: Plot of maximum of the absolute value of electric field $|E|_{max}$ with time, on a 128×128 gridsize.

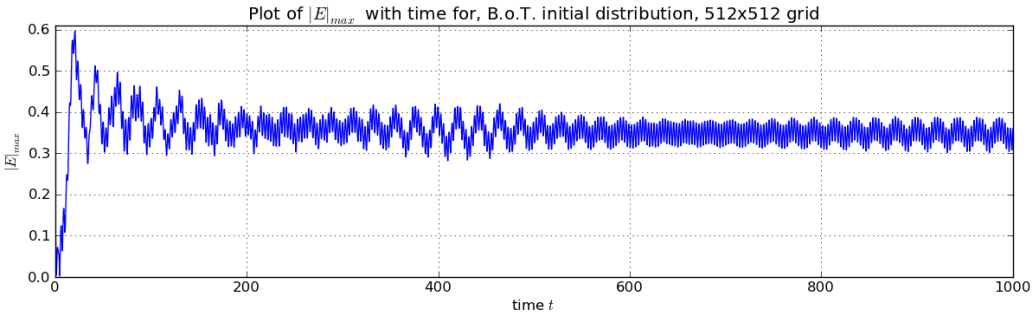

Figure B.13: Plot of maximum of the absolute value of electric field $|E|_{max}$ with time, on a 512×512 gridsize.

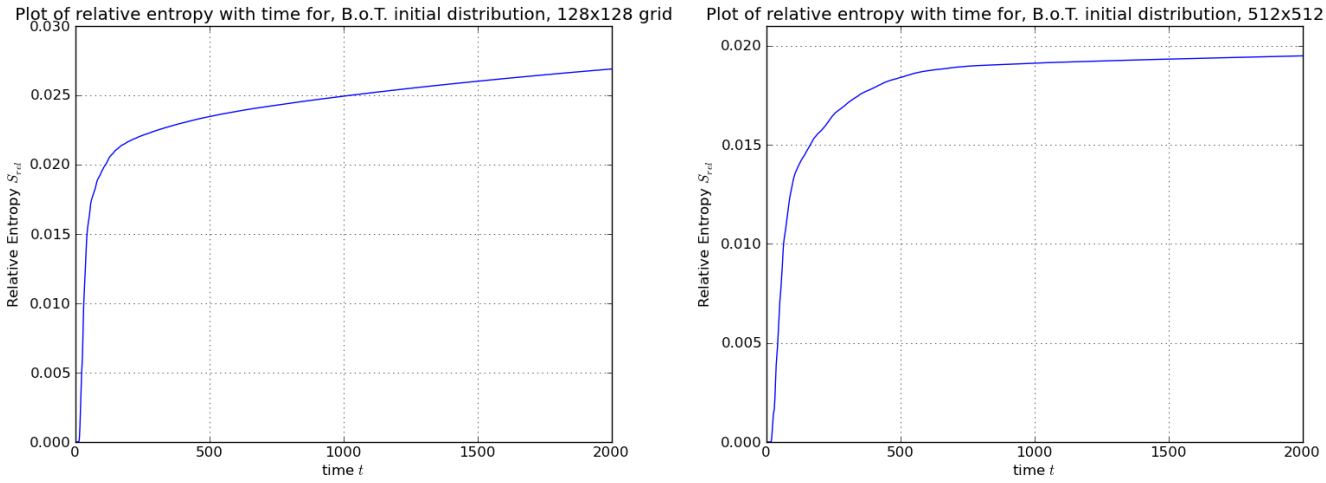

(a) 128×128 grid.

(b) 512×512 grid.

Figure B.14: Relative entropy S_{rel} plotted with time t.

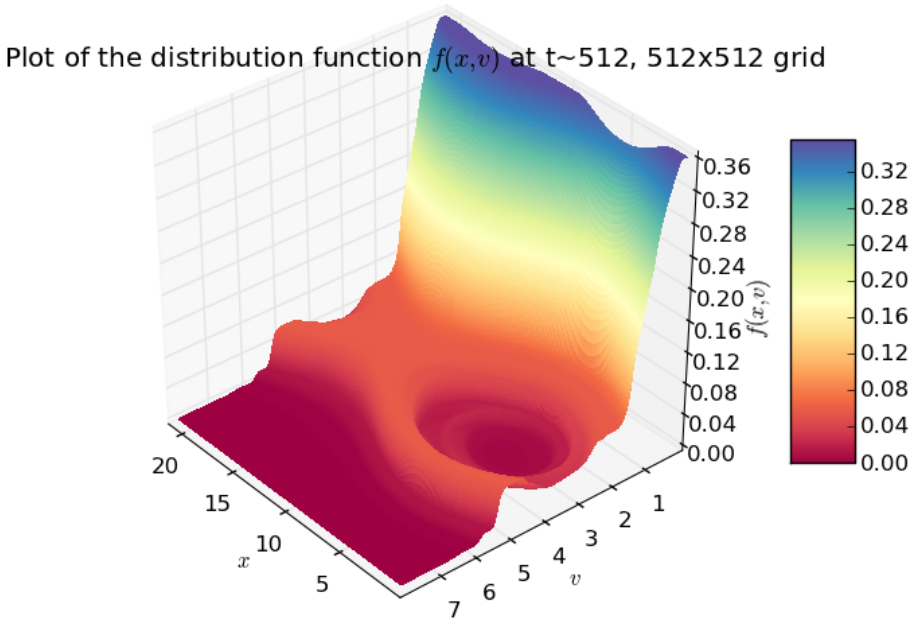

Figure B.15: Plot of the distribution function $f(x, v, t)$, at $t \sim 512$, around the region of the perturbation.

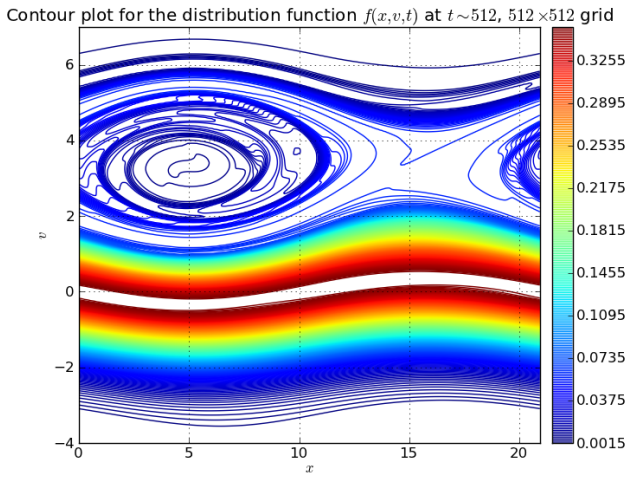

(a) $t \sim 512$

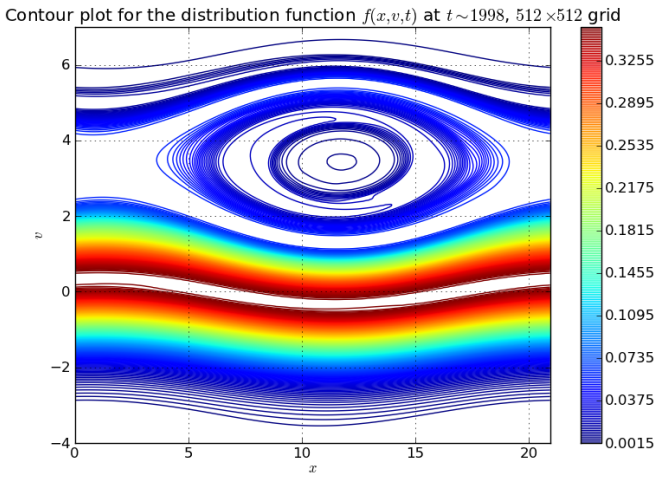

(b) $t \sim 1998$

Figure B.16: 2d contour plots for the distribution function $f(x, v, t)$ at two different times in the simulation. The phase-space holes are in different positions because of the constant movement along x.

One can compare this plot to the Fig. 6 in Arber and Vann[22]. Furthermore, the 2d contour plots for the distribution function $f(x, v, t)$ at two different times in the simulation are in Fig. B.16. One can see the evolution of the phase space hole and how this hole smoothens out with time. This phase space hole represents a potential energy trough. One can see this from the plots of the electric field at different times, as shown in figure B.17. Now, from the plot of maximum amplitude of electric field (Fig. B.13), one can see that landau damping doesn't happen here and the electric field settles to oscillating around a non-zero value. This oscillation corresponds to periodic trapping and untrapping of particles. One can see this through the electric field plot too, that the particles inside the phase space hole face a restoring force that tends to keep them inside the hole. Particularly, at the center of the phase space hole, particles essentially face no restoring force, i.e. they are trapped at the center. Now, for a fraction of particles at the boundary (separatrix) of the phase-space hole may escape or enter depending on their energy. This process acquires a periodicity, and is referred to as a BGK mode. We wish to, in future, study the properties of particles near the separatrix of the phase space hole, in order to understand the BGK mode further. Also, BGK mode, such as the one obtained, is a travelling wave solution.

Now, we check the plots of the velocity distribution function to see its form at $t \sim 2000$. This has been plotted in figure (B.18). It can be seen that the function for the 512×512 has damped and is almost flat, whereas the other isn't yet. This is supported by the observations from the entropy curve.

Now we would like to see the effect of the large timestep algorithm on the B.o.T. simulation. Since the 512×512 grid simulation stabilizes much before $t = 2000$, we run

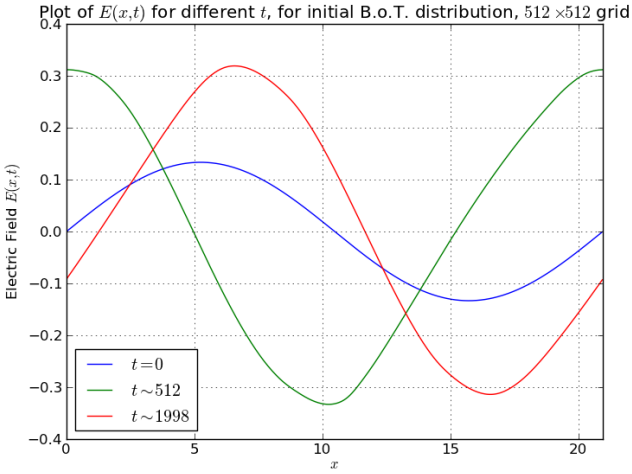

Figure B.17: Plots of the electric field $E(x,t)$ at different t. One can see how electric field becomes zero at the value of x corresponding to the centre of the phase space hole in Fig. B.16.

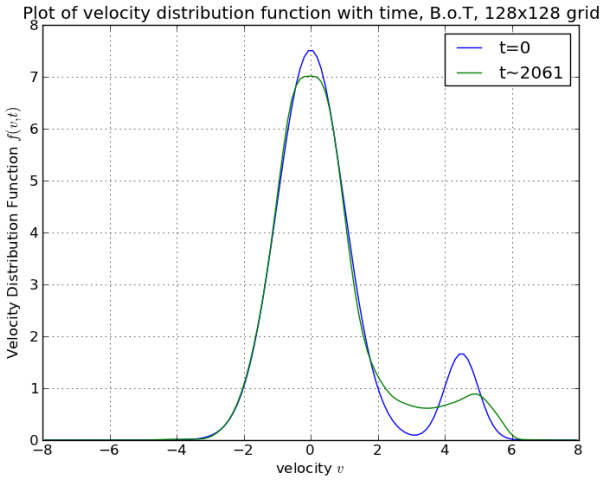

(a) 128×128 grid.

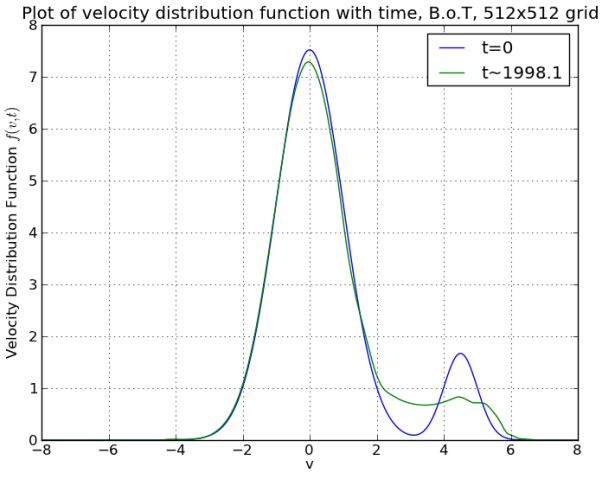

(b) 512×512 grid.

Figure B.18: Velocity distribution function $f(v)$ for both gridsizes tested.

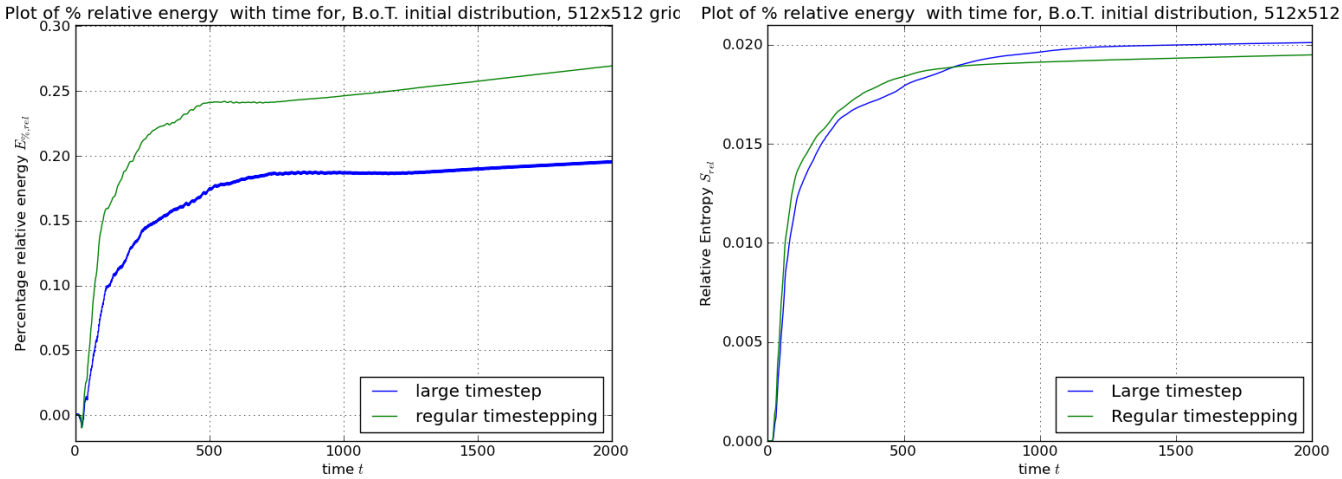

(a) Percent relative energy $E_{\%,rel}$

(b) Relative entropy S_{rel}

Figure B.19: Comparison between large timestepping and regular timestepping, for B.o.T. initial conditions. For 512×512 grid.

with this. We choose $\Delta t = 0.1$, and rerun the program for the same initial conditions. We plot the graphs for percent relative energy and relative entropy, comparing both the large timestepping and the regular timestepping (figure (B.19)). One can see that the entropy curve of the large timestep almost remains the same as the regular one. However, one can see an advantage in energy conservation, as the error from the Strang splitting is compensated by the smaller number of timesteps needed, and hence, accumulating lesser error from the PPM advection routine. We have also plotted the velocity distribution function for both the timestep methods at $t \sim 2000$ (figure (B.20)). One can see that there is no visible difference between the two curves. Note that the curves are from slightly times, due to the choice of number of dumps in the file writing algorithm. Although it has not been shown, the evolution of the maximum absolute amplitude of the electric field $|E|_{max}$ also looks similar to Fig. B.13.

Now that we have benchmarked the Vlasov-Poisson solver for different initial conditions, we move on to one more benchmark that involves the large timestep algorithm.

B.3 Nonlinear Landau Damping

As mentioned before, linear landau damping fails after the bounce time $\tau = 2\pi/\alpha$. Beyond this time, the landau damping phenomenon is inherently nonlinear. O'Neil has given an approximate solution, but it too breaks down over large times[7, 4]. It is an open problem to understand the behaviour of nonlinear landau damping over long times. Bernstein-Greene-Kruskal have suggested that the plasma waves finally settle to a steady state (called the BGK steady state)[7, 5]. On the other hand, Isichenko has expressed, as a general result, that Landau damping continues indefinitely though the damping is

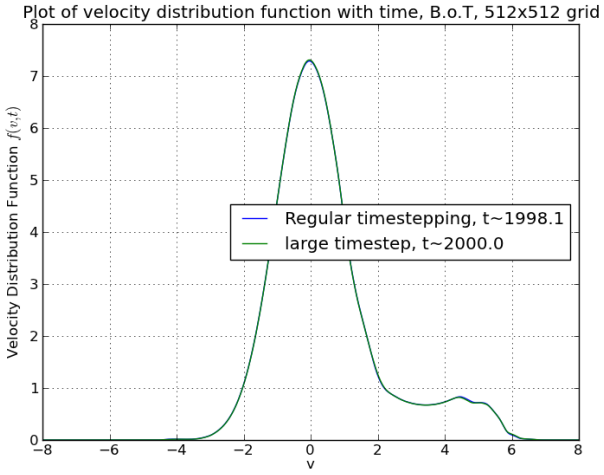

Figure B.20: Plot of the velocity distribution function $f(v)$ for both the timestep methods.

algebraic (i.e. a power of t), not exponential[7, 6]. Manfredi has shown, through numerical simulations, that contrary to Isichenko's predictions, there exist initial conditions in which the system settles to a BGK mode[7]. Manfredi further states that Isichenko's assumption that the electric field decays to zero by Landau damping, is crucial to finding the functional form of such a decay[7]. Further, Firpo and Elskens have studied Landau damping in the regime of a second order phase transition, and have found a critial initial wave intensity, under which the wave amplitude vanishes and over which the damping leads to a finite wave amplitude[9]. Thus, this phenomenon is an open problem. We study this phenomenon with the same initial distribution function, as in Manfredi[7].

The initial distribution function is chosen to be:

$$f(x, v, 0) = (1 + \alpha \cos(kx)) \exp(-v^2/2) \tag{B.14}$$

and this time, the parameters chosen are:

$$v^e_{max} = 6,\ \alpha = 0.05,\ k = 0.4 \tag{B.15}$$

Now the problem is to see how nonlinear landau damping behaves at large times (of up to $t = 2000$)[7]. As the perturbation is still small, the main problem is to push away recurrence as away as possible. For this reason the runs are configured with $N_v = 4000, 8000$, which makes $T_R \sim 5236, 10472$ respectively. As we know with linear landau damping, our runs can be considered accurate up to time $T_R/2$. Since $T_R/2 > 2000$ for both the cases, recurrence related effects are not a worry within this time domain. Also, N_x is chosen to have values of $N_x = 512, 1024$ for the high resolution needed in x. Also, $\Delta t = 0.1$, which leads to a maximum CFL number of $k = 19.55, 39.11$ respectively, both well within our empirical limit of 5% of N_x. (One can note that Manfredi[7] called the choice of $\Delta t = 0.1$ "conservative" as compared to the value of $\Delta t = 0.25$ used by Ghizzo, et al[26]. This is also supported by our observations.)

Three runs are given, the first one with gridsize 512×4000, the second one 512×8000 and the third one 1024×4000. The initial conditions and the runs have been chosen exactly the same as Manfredi, so as to compare the results. As we did with linear landau damping, we now plot the amplitude of the fundamental harmonic $|E_k|$ with time for the three runs (Fig. B.21)

These plots are quite similar, for want of better words, to Fig. 1 of Manfredi[7]. One can notice slightly more detail in (b) than in the other two. It may be because of larger N_v. Other than this, one cannot observe any qualitative difference in the plots.

Now, we compare the relative entropy and percent relative energy for the three runs (Fig. B.22). It can be seen that the relative entropy curves, with the exception of the near "overlap" of the first and third run, is similar to Fig. 2 from Manfredi[7]. Also, energy is conserved, in the second case to within 0.005% and within 0.012% for the first and third.

Now, we would like to see the phase-space resonant region, like in the case of B.o.T.. So, we plot a colormap plot of the distribution function at $t = 1600$ (Fig. B.23), for the first run (512×4000 gridsize). This also qualitatively looks similar to Fig. 3 from Manfredi[7]. Again, we would like to look at the nature of the velocity distribution function. To exaggerate the resonant region, we plot the logarithm (base 10) of the normalized velocity distribution function. This can be seen in figure (B.24) Again this is similar to Fig. 4 of Manfredi[7]. It can also be seen that the second harmonic gets quickly excited and then falls to the order of 10^{-4} (Fig. B.25). Next, we excite two modes $k = 0.2$ and $k = 0.4$, with the initial condition:

$$f(x, v, 0) = (1 + \alpha \cos(0.2x) + \alpha \cos(0.4x)) \exp(-v^2/2) \tag{B.16}$$

with $L = 2\pi/0.2$ and rest of the parameters remaining the same. This is in order to regenerate Manfredi's results with two excited modes. The plots for the amplitudes of fundamental and second harmonic of the electric field are in figure (B.26) As Manfredi states, the first harmonic remains undamped and the second harmonic behaves like our previous case, albeit settling to a smaller value than before[7].

Thus, in this subsection, we have used large timestep algorithm (which was benchmarked in the previous subsections) to run long time simulations. We have, in this process, confirmed the validity of our algorithm by replicating Manfredi's results step-by-step.

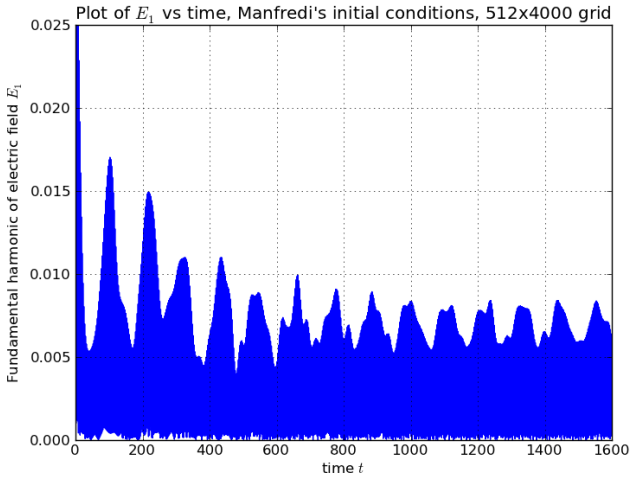

(a) 512×4000 grid.

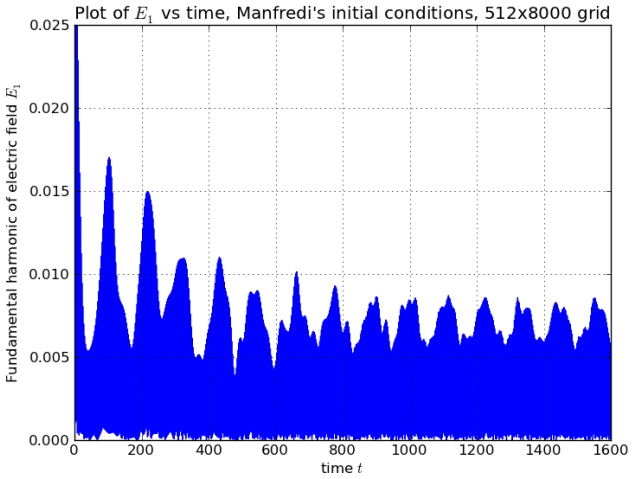

(b) 512×8000 grid.

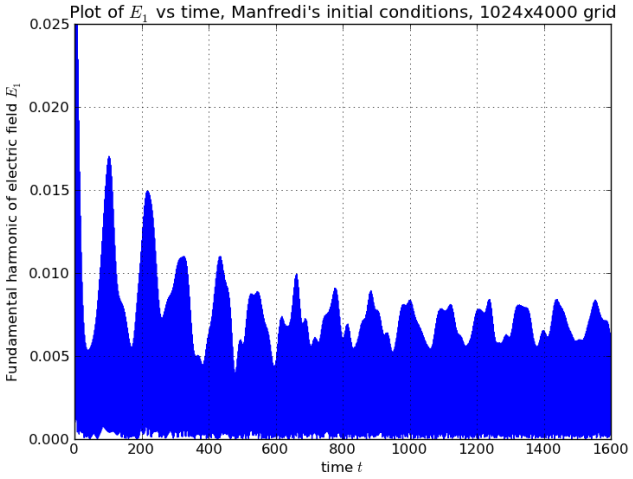

(c) 1024×4000 grid.

Figure B.21: Plot of the amplitude of the fundamental harmonic of the electric field $|E_k|$ vs time, for Manfredi's initial conditions.

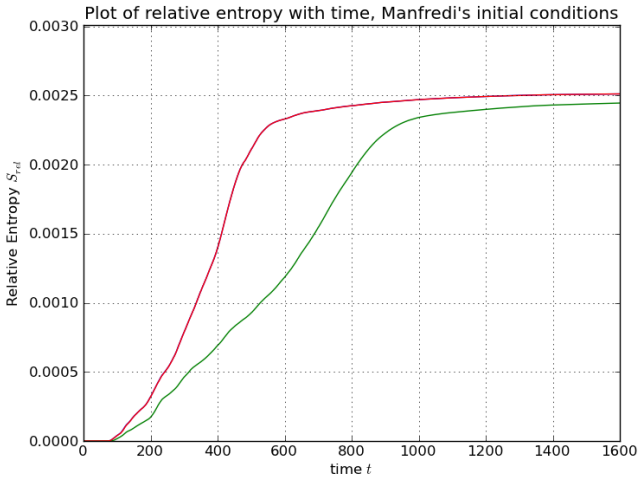

(a) Relative entropy S_{rel} vs time

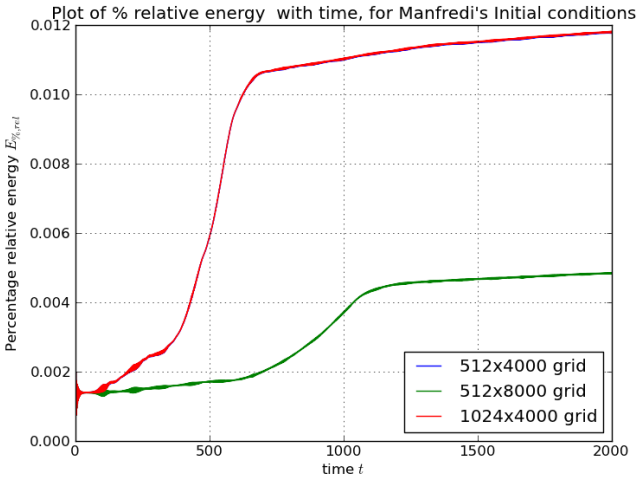

(b) Percent relative energy $E_{\%,rel}$ vs time

Figure B.22: Plots for the three runs. The plots for the 512×4000 and 1024×4000 fall close together, and hence appear as a single curve. They are slightly spaced apart.

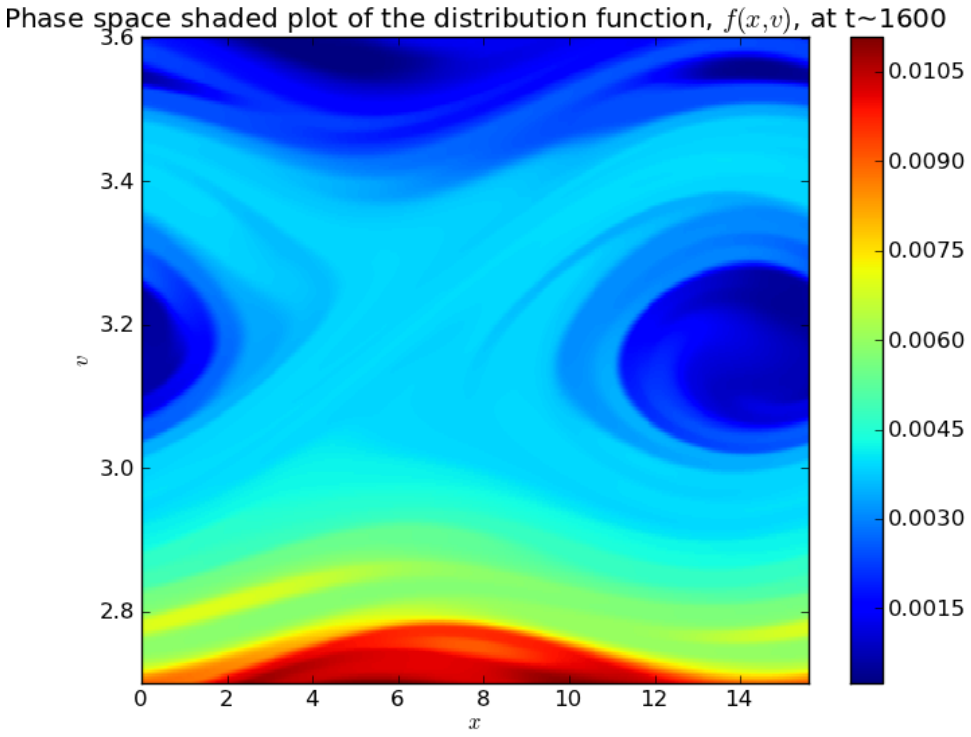

Figure B.23: Plot of the resonant region of the distribution function, for run on the 512×4000 gridsize, at $t = 1600$.

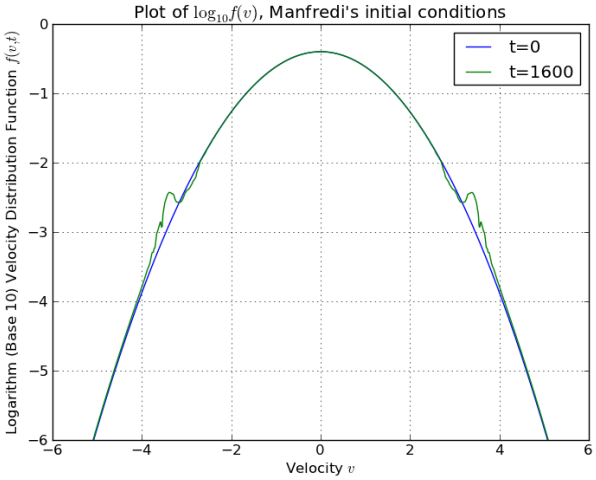

Figure B.24: Plot of the logarithm (base 10) of the normalized velocity distribution function, for run on the 512×4000 gridsize, at $t = 0, 1600$.

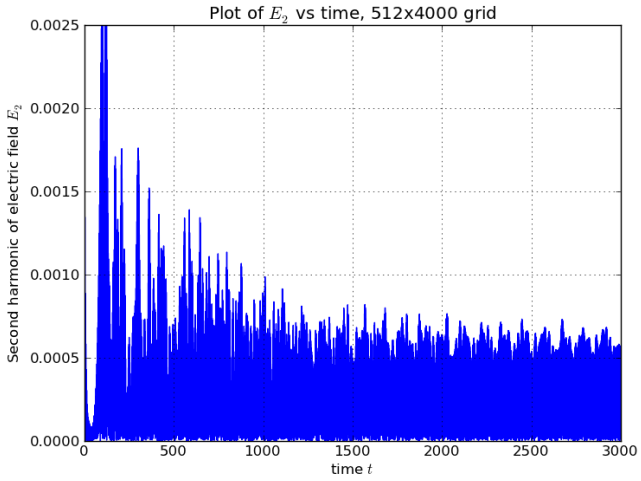

Figure B.25: Plot of the second harmonic of the electric field $|E_2|$ vs time, for 512×4000 grid. One can see that it quickly gets excited from zero and then settles at around 0.5×10^{-4}.

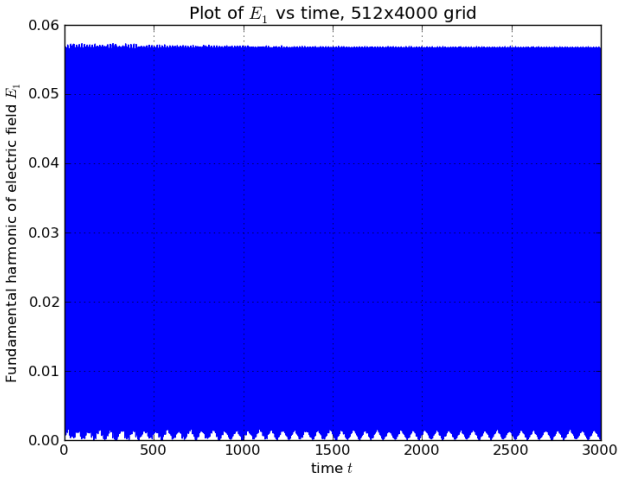

(a) Plot of $|E_1|$ with time

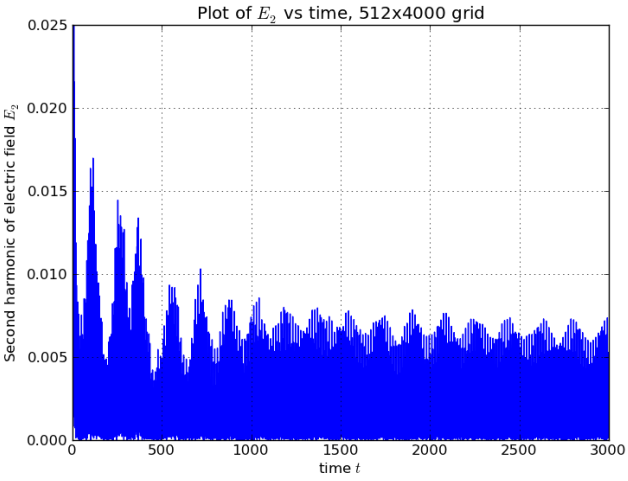

(b) Plot of $|E_2|$ with time

Figure B.26: Plots for time evolution of fundamental and second harmonics of electric field with time.